


Article

Advanced Torque Ripple Minimization of Synchronous Reluctance Machine for Electric Vehicle Application

Olaoluwa Demola Aladetola ¹, Mondher Ouari ¹, Yakoub Saadi ², Tedjani Mesbahi ²,
Moussa Boukhnifer ^{3,*} and Kondo Hloindo Adjallah ¹

¹ Laboratoire de Conception, Optimisation et Modélisation des Systèmes, Université de Lorraine, 57000 Metz, France

² ICube, CNRS (UMR 7357) INSA Strasbourg, University of Strasbourg, 67000 Strasbourg, France

³ Université de Lorraine, LCOMS, 57000 Metz, France

* Correspondence: moussa.boukhnifer@univ-lorraine.fr

Abstract: The electric machine and the control system determine the performance of the electric vehicle drivetrain. Unlike rare-earth magnet machines such as permanent magnet synchronous machines (PMSMs), synchronous reluctance machines (SynRMs) are manufactured without permanent magnets. This allows them to be used as an alternative to rare-earth magnet machines. However, one of the main drawbacks of this machine is its high torque ripple, which generates significant acoustic noise. The most typical method for reducing this torque ripple is to employ an optimized structural design or a customized control technique. The objective of this paper is the use of a control approach to minimize the torque ripple effects issue in the SynRM. This work is performed in two steps: Initially, the reference current calculation bloc is modified to reduce the torque ripple of the machine. A method for calculating the optimal reference currents based on the stator joule loss is proposed. The proposed method is compared to two methods used in the literature, the FOC and MTPA methods. A comparative study between the three methods based on the torque ripple rate shows that the proposed method allows a significant reduction in the torque ripple. The second contribution to the minimization of the torque ripple is to propose a sliding mode control. This control suffers from the phenomenon of “Chattering” which affects the torque ripple. To solve this problem, a second-order sliding mode control is proposed. A comparative study between the different approaches shows that the second-order sliding mode provides the lowest torque ripple rate of the machine.

Keywords: electric vehicle; synchronous reluctance machine; field-oriented control; maximum torque per ampere; optimal current calculation; sliding mode control; torque ripple minimization



Citation: Aladetola, O.D.; Ouari, M.; Saadi, Y.; Mesbahi, T.; Boukhnifer, M.; Adjallah, K.H. Advanced Torque Ripple Minimization of Synchronous Reluctance Machine for Electric Vehicle Application. *Energies* **2023**, *16*, 2701. <https://doi.org/10.3390/en16062701>

Academic Editor: King Jet Tseng

Received: 10 February 2023

Revised: 5 March 2023

Accepted: 7 March 2023

Published: 14 March 2023



Copyright: © 2023 by the authors. Licensee MDPI, Basel, Switzerland. This article is an open access article distributed under the terms and conditions of the Creative Commons Attribution (CC BY) license (<https://creativecommons.org/licenses/by/4.0/>).

1. Introduction

The rapid increase in the number of conventional vehicles has led to a significant increase in greenhouse gas emissions, the depletion of fossil fuels, and various negative consequences for the people living in these environments [1]. Unlike conventional vehicles, which face the problem of fuel poverty, electric vehicles (EVs) can have significant emissions and environmental benefits over conventional vehicles. As well, they can significantly reduce fuel costs due to the high efficiency of electric drive components [2].

The electrification of the automotive sector is accelerating, and carmakers and equipment manufacturers are reinventing electric machines to adapt them to the constraints of electric drivetrains. A high power density, high torque density, wide speed range, and efficiency are critical factors in the selection of electric motor technology for this application [3]. Permanent magnet synchronous machines (PMSMs) are by far the most widely utilized electric machine technology in the electric vehicle (EV) market [4].

In 2021, PMSMs accounted for 84% of the electric car market [5]. However, the magnets used in these machines are typically rich in rare-earth materials (REMs), primarily

Neodymium, but also often contain a range of heavy rare earth, such as Dysprosium [6,7]. Nevertheless, the cost of REM-based machines has increased over several years. Furthermore, due to restricted resources, the use of REM-based machines in EV applications is now being challenged [8].

The above factors have prompted several equipment manufacturers to design rare-earth-free machines, such as Renault's wound rotor synchronous machine (WRSM) in the ZOE and the Audi induction machine (IM) in its e-tron models [9,10]. Due to the robustness, simplicity of fabrication, small size, and compatibility with the requirements of the EV electric machine, the synchronous reluctance machine (SynRM) is an alternative for REM-based machines. The SynRM has a wound stator that has neither conductors nor magnets like the IM and it operates like a WRSM without a DC field winding in its rotor [11]. Moreover, the power converter used to supply this machine is a three-phase inverter, which facilitates the replacement of the IMs and PMSMs without a specific power converter. Figure 1 illustrates a simplified architecture of the essential components of an electric vehicle propelled using a synchronous reluctance machine.

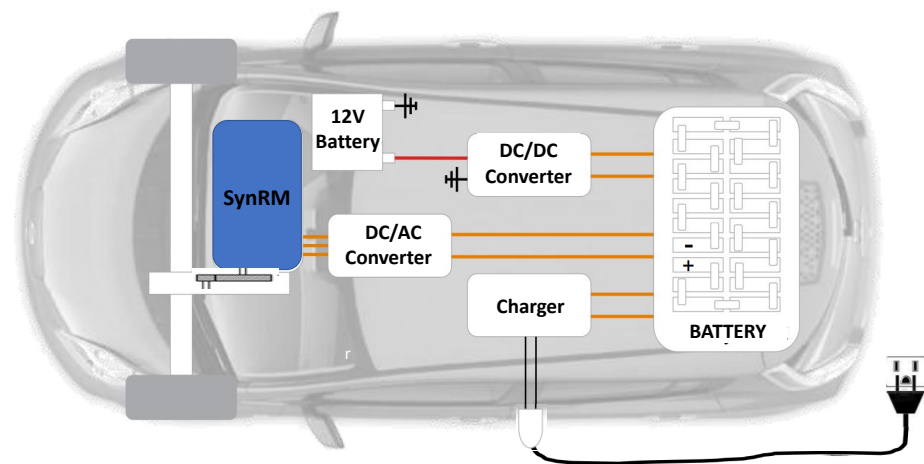


Figure 1. Simplified electric vehicle drivetrain architecture propelled by a SynRM.

However, the nonlinear magnetic path of the SynRM and the operational saturation of the rotor core segments cause significant torque ripples and acoustic noise [12,13]. However, these drawbacks can be significantly reduced with an optimal structure design [14,15] and/or a good control strategy [16–18]. The optimization of flux barriers [19,20], rotor ribs [21,22], rotor skewing [23,24], and adding permanent magnets [25,26] is the most common strategy for an optimal structural design. Although optimizing the SynRM structure may offer satisfactory results, the design procedure is typically time-consuming.

The focus of this research is on control-based strategies for minimizing the torque ripple of the SynRM. Several strategies to reduce the torque ripple effect of the machine have been investigated in the literature.

The authors of the publication [11] present a general review of various control scheme strategies for SynRM's current regulation. This research examines the designs, techniques, benefits, and drawbacks of synchronous reluctance machine control systems, such as direct torque control (DTC), field-oriented control (FOC), predictive control, and many others. This study demonstrates the limitations of each method for reducing the torque ripple effect in a synchronous reluctance machine. The DTC method provides high dynamic control, which makes it superior to other methods [11]. Because it does not use a current controller, this approach achieves a substantially superior transient torque control performance. Furthermore, it controls the machine solely by stator resistance, resulting in reasonably robust machine control with quick dynamics. This method is appropriate for specifications that require a better transient response rather than a steady-state response for control [27]. Nevertheless, this method generates significant torque ripples as compared to other approaches, and its implementation necessitates the use of a torque sensor or an extra

sensorless torque block solution [28]. This adds significant computing time. Furthermore, because this method uses a variable switching frequency to control the flux, it produces a relatively high harmonic current and high torque ripples, causing significant noise levels in the machine. In reference [29], the torque ripples were handled satisfactorily in the DTC technique using multilevel inverters. Moreover, a mechanism is created and employed to limit the torque in [27–29]. In this technique, the torque-limiting mechanism adjusts the flux reference with respect to the torque error sign to ensure a steady machine operation.

A field-oriented control (FOC) strategy is proposed in [30] to achieve convenient control of the SynRM. This method controls the SynRM in the d, q reference frame, representing the machine as a direct current (DC) machine. In this review, FOC is categorized into two techniques for controlling decoupling currents i_d, i_q in the synchronous reference frame: direct field-oriented control (DFOC) and indirect field-oriented control (IFOC). This method features a precise control method, reduced torque ripples in comparison to the DTC method, improved steady-state responsiveness, and a consistent switching frequency, which makes it attractive to researchers because of its high steady-state performance [30].

Another control-based method for reducing the SynRM torque ripple is to add specified current harmonics to the original sinusoidal stator currents. The authors of [31] investigated the average torque of a two-phase SynRM and defined the optimal current using different stator inductance harmonics. Each torque harmonic requires multiple current harmonics to be reduced. When numerous dominant torque harmonics are taken into account, the process of determining the link between each torque harmonic and the corresponding current harmonics can become lengthy and difficult. Therefore, the suggested method makes determining the appropriate currents for a multiphase SynRM extremely challenging. The stator inductances and low-order harmonics are measured in [32] to determine the optimal currents using the electromagnetic torque equation. But nonetheless, measuring the high-order stator inductance harmonics accurately is extremely difficult. This means the optimal currents determined by measured inductances may not result in the most effective torque ripple reduction. Some strategies for reducing torque ripples rely on a reference currents calculation bloc. This bloc's purpose is to generate reference currents via the reference torque [16]. To minimize the torque ripple, the active torque ripple cancellation control technique is examined in [33]. To provide a smooth output torque, the active torque ripple cancellation method actively regulates the excitation of current waveforms using torque to the current function. The term “active” refers to a method for canceling the torque ripple of the machine while it is functioning at a varied torque-speed range.

This paper will address the problem of the torque ripple minimization of a synchronous reluctance machine used in electric vehicle propulsion. Based on a velocity/current cascade control strategy, we first suggest changing the reference currents calculation bloc, which transforms the reference torque into reference currents via a stator current optimization method. In other words, the torque ripple can be reduced by optimizing the reference currents because stator currents represent the machine's torque. To assess the efficacy of the suggested method, we will replicate the reference currents calculation investigated in the literature, namely the control by flux-oriented control (FOC) and maximum torque per ampere (MTPA) with PI control. The torque ripple ratio of each method is then examined in a comparative study.

Secondly, based on the velocity/current cascade control, the optimal currents calculations method from the first study will be chosen. We propose nonlinear controls to replace the PI control, notably the classical sliding mode control, and the second-order sliding mode control, to improve the stator current control and hence the torque ripple minimization. The performance of each control approach is then compared, along with the torque ripple ratio.

The structure of this article is as follows: Section 2 explains the modeling and behavior of the synchronous reluctance machine, as well as the velocity/current cascade control strategy. The reference currents calculation bloc description utilizing the FOC, the MTPA

control, and the suggested optimal current computation approach are covered in Section 3. In Section 4, the proposed classical and second-order sliding mode controllers are combined with the optimal reference currents calculation method. Section 5 contains the conclusions that bring this article to a close.

2. SynRM Modeling and Description of the Velocity/Currents Cascade Control Strategy

In this section, the description of the modeling, as well as the velocity/currents control strategy used in driving the synchronous reluctance machine in this work are presented.

2.1. SynRM Modeling

The synchronous reluctance machine is a pure AC machine that requires a polyphase sinusoidal AC current. The torque of this machine is produced by a difference in magnetic conductivities along the direct axes of the rotor, as well as by the quadrature, which lacks permanent magnets and field windings [34,35]. The SynRM used in this work is a three-phase flux barrier type with four-pole machine as shown in Figure 2a.

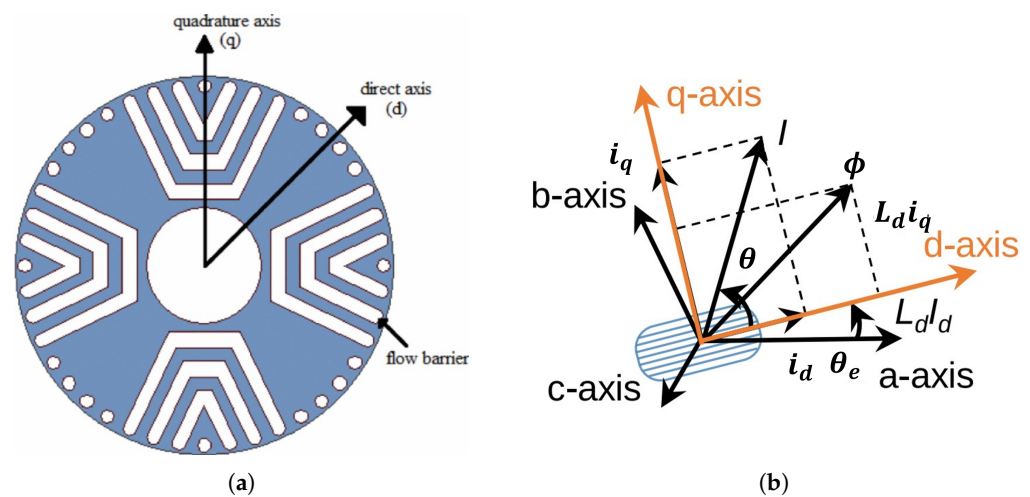


Figure 2. (a): Cross section of an exemplary SynRM with four poles. (b): Transformation of the system in synchronous (dq) reference frame [36].

2.1.1. Electric Model

SynRM's electrical model is based on the following assumptions [37]:

- Magnetic materials are isotropic and non-saturable.
- The hysteresis effect and iron losses are neglected.
- The inductance variations are sinusoidal (first harmonic hypothesis).
- The capacitive coupling between the machine's windings is ignored.

Given the assumptions, the voltage v applied to a phase is equal to the resistive voltage drop across the phase winding plus the flux change beneath a rotor pole and is denoted by

$$\begin{cases} v = R_s i + \frac{d\Phi}{dt} \\ \Phi = L(p\theta) \cdot i \end{cases} \quad (1)$$

where

- $v = [v_a \ v_b \ v_c]^T$: the stator voltage vector;
- $i = [i_a \ i_b \ i_c]^T$: the stator current vector;
- $\Phi = [\Phi_a \ \Phi_b \ \Phi_c]^T$: the vector of the total fluxes through the windings $a - b - c$;
- R_s : the resistance of a stator phase;
- θ and p : the mechanical position and the number of pole pairs, respectively;

- $L(p\theta)$: the stator inductance matrix given by [38]

$$L(p\theta) = \begin{bmatrix} L_a(p\theta) & M_{ab}(p\theta) & M_{ac}(p\theta) \\ M_{ba}(p\theta) & L_b(p\theta) & M_{bc}(p\theta) \\ M_{ca}(p\theta) & M_{cb}(p\theta) & L_c(p\theta) \end{bmatrix} \quad (2)$$

With L_i is the stator inductance of phase i and M_{ij} is the mutual inductance between phases i and j ($i, j = (a, b, c)$) [38,39].

The electrical equations in the $d-q$ frame (see Figure 2b), in the absence of a zero sequence current component, are given by [40–42]

$$\begin{cases} v_{ds} = R_s i_{ds} + \frac{d\Phi_{ds}}{dt} - p\Omega\Phi_{qs} \\ v_{qs} = R_s i_{qs} + \frac{d\Phi_{qs}}{dt} + p\Omega\Phi_{ds} \end{cases} \quad (3)$$

with the following:

- v_{ds} and v_{qs} are the stator voltage in the d and q axes.
- Ω is the machine velocity.
- Φ_s , Φ_{qs} , and Φ_{ds} are the total stator and flux linkage in the d and q axes given by

$$\begin{cases} \Phi_{ds} = L_d i_{ds} \\ \Phi_{qs} = L_q i_{qs} \\ \Phi_s = \sqrt{\Phi_{ds}^2 + \Phi_{qs}^2} \end{cases} \quad (4)$$

- L_d , L_q are the d and q -axes stator inductances.

Finally, the voltage equations can be written as follows:

$$\begin{bmatrix} v_{ds} \\ v_{qs} \end{bmatrix} = R_s \begin{bmatrix} i_{ds} \\ i_{qs} \end{bmatrix} + \begin{bmatrix} L_d \\ L_q \end{bmatrix} \frac{d}{dt} \begin{bmatrix} i_{ds} \\ i_{qs} \end{bmatrix} + p\Omega \begin{bmatrix} 0 & -L_q \\ L_d & 0 \end{bmatrix} \begin{bmatrix} i_{ds} \\ i_{qs} \end{bmatrix} \quad (5)$$

2.1.2. Electromechanical Model

The electromagnetic torque of the SynRM can be expressed by [42]

$$T_e = p(L_d - L_q)i_{ds}i_{qs} \quad (6)$$

From the electromagnetic torque equation, the fundamental relation of the dynamics of the rotating part of the machine is given by [40–42]

$$\frac{d\Omega}{dt} = \frac{1}{J}(T_e - T_r - f_r\Omega) \quad (7)$$

- Ω : rotational velocity of the machine, in rad/s.
- T_e : electromagnetic torque produced by the machine, in Nm.
- T_L : load torque, in Nm.
- f_r : viscous friction coefficient, in Ns^2/m^2 .

The SynRM state model in $d - q$ is finally written as follows:

$$\frac{d}{dt} \begin{bmatrix} i_{ds} \\ i_{qs} \\ \Omega \\ \theta \end{bmatrix} = \begin{bmatrix} -\frac{R_s}{L_d} i_{ds} + p\Omega \frac{L_q}{L_d} i_{qs} \\ -\frac{R_s}{L_q} i_{qs} + p\Omega \frac{L_d}{L_q} i_{ds} \\ \frac{3}{2} p \frac{(L_d - L_q)}{j} i_{ds} i_{qs} - \frac{f_r}{j} \Omega - \frac{T_r}{j} \\ \Omega \end{bmatrix} + \begin{bmatrix} \frac{1}{L_d} & 0 \\ 0 & \frac{1}{L_q} \\ 0 & 0 \\ 0 & 0 \end{bmatrix} \begin{bmatrix} V_{ds} \\ v_{qs} \end{bmatrix} \quad (8)$$

2.1.3. Vehicle Load Torque Modeling

Figure 3 shows the driving force and the mean forces resistant to the advance of a vehicle in a slope α [43].

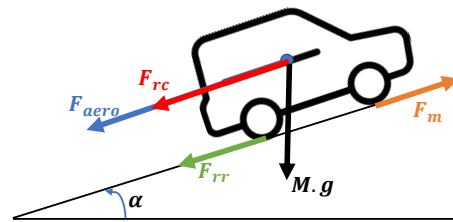


Figure 3. The typical driving force and resisting forces components of a vehicle [43].

where

- F_m : the slope force or tractive force that is required to drive the vehicle up.
- F_{aero} : the aerodynamic force created by the friction of the vehicle's body moving through the air.
- F_{rr} : the rolling resistance force.
- F_{rc} : the resistance force exerted by the vehicle weight as it goes up and down a hill.
- M : the vehicle mass.
- g : the acceleration due to gravity on Earth.

The expression of each resisting force is given by [44]

$$\begin{cases} F_{aero} = \frac{1}{2} \rho c_x s_f V^2 \\ F_{rr} = f_{rr} m g \cos(\alpha) \\ F_{rc} = m g \sin(\alpha) \end{cases} \quad (9)$$

where

- ρ : the density of the air, in kg/m^3 .
- c_x : the drag coefficient.
- s_f : frontal cross-sectional area, in m^2 .
- f_{rr} : rolling resistance value, in N.

From [44–46], the linear speed of a vehicle V can be expressed using different forces as follows:

$$M \frac{dV}{dt} = F_m - F_{aero} - F_{rr} - F_{rc} \quad (10)$$

Because $V = R_{sc} \Omega$ where R_{sc} is the resistance of the EV in a slope.

The total load torque of the vehicle T_r in the steady state can be written from the Equation (9) by

$$T_r = \frac{1}{2} \rho c_x s_f R_{sc}^3 \Omega_{sc}^2 + m g R_{sc} [\sin(\alpha) + f_{rr} \cos(\alpha)] \quad (11)$$

2.2. SynRM Cascade Control Strategy

Figure 4 shows the cascade velocity / currents control strategy used in this study [47]. The EV driver is presented by a velocity controller that provides the reference torque T_e^* . An indirect torque control approach is used to regulate the machine's torque by regulating the stator currents given by i_d^* and i_q^* . The reference currents calculation bloc is used to transform the reference torque into reference currents i_d^* and i_q^* . These currents are then controlled in the internal control loop.

This strategy allows torque to be controlled indirectly by controlling the currents and provides a separation between the electrical and mechanical variables.

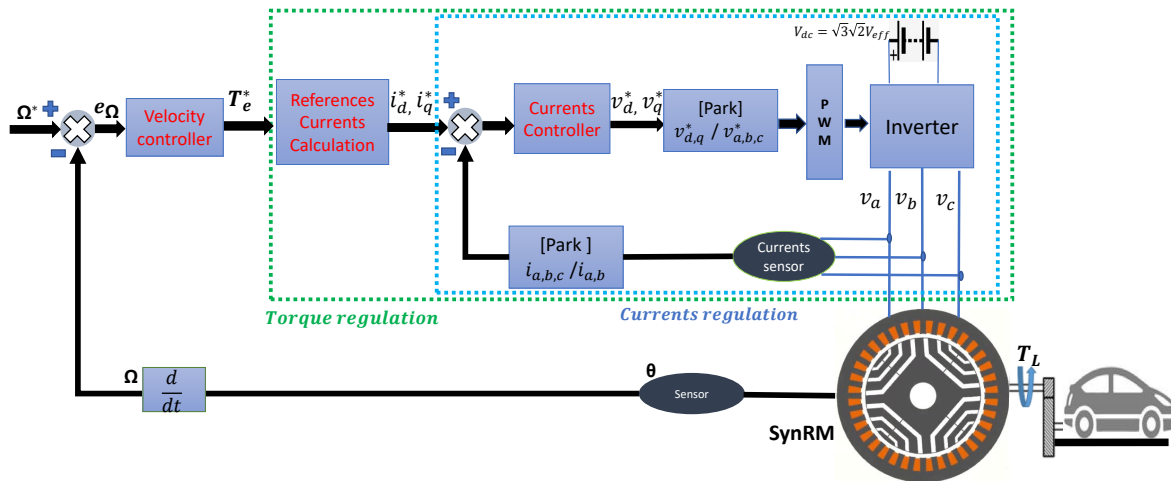


Figure 4. Block diagram of the cascade velocity / currents control strategy [47].

3. Torque Ripple Minimization by Using the Currents References Calculation

In this section, different techniques for calculating current reference in the reference currents calculation bloc have been adopted, to study the effect of currents on torque ripple and control output.

3.1. Conventional Field-Oriented Control (FOC)

The conventional field-oriented control of the synchronous machine controls the current with respect to the reference current which automatically controls the torque by using only one component of the current and by setting the other to a constant (zero in the case of a permanent magnet synchronous machine) [48]. Analogously, this command consists of imposing a constant value on one component of the current and allowing the other component to regulate the torque given that the expression of the electromagnetic torque of the machine in the reference ($d-q$) is

$$T_e = p(L_d - L_q)i_{d_s}i_{q_s} \quad (12)$$

By imposing the reference of the component i_d to a constant,

$$i_d^* = c^{te} \quad (13)$$

From (12) and (13), the reference of the component i_q can be calculated as follows:

$$i_q^* = \frac{T_e^*}{p(L_d - L_q)i_d^*} \quad (14)$$

3.2. Maximum Torque per Ampere (MTPA)

MTPA or maximum torque per ampere operation is the most preferred operating mode for any motor operating with the vector control [49].

This method provides the maximum torque for a given operating current. This method controls both currents i_d and i_q . The operating condition at the maximum point can be deduced from the electromagnetic torque equation:

$$T_e = p(L_d - L_q)i_{ds}i_{qs} \quad (15)$$

Assuming sinusoidal stator currents, Park's transformation allows us to write

$$\begin{cases} i_{ds} = \sqrt{\frac{3}{2}} I_s \sin \gamma \\ i_{qs} = \sqrt{\frac{3}{2}} I_s \cos \gamma \end{cases} \quad (16)$$

with I_s the amplitude of the stator current and $\gamma = \omega t + \varphi$, where ω and φ are the electrical network pulsation in rad/s and phase at the reference origin in rad, respectively. Thus, from Equations (15) and (16), the expression of the electromagnetic couple becomes

$$T_e = \frac{3}{2} p(L_d - L_q) I_s^2 \sin \gamma \cos \gamma \quad (17)$$

Knowing that $\sin \gamma \cos \gamma = \frac{\sin 2\gamma}{2}$, the expression of the electromagnetic torque becomes

$$T_e = \frac{3}{2} p(L_d - L_q) I_s^2 = \frac{\sin 2\gamma}{2} \quad (18)$$

Then, the condition for the maximization of torque per ampere can be written as

$$\left. \frac{dT_e}{d\gamma} \right|_{I_s=cte} = \frac{3}{2} p(L_d - L_q) I_s^2 \cos 2\gamma = 0 \quad (19)$$

Solving the Equation (15) allows finding the expression of the components of the current as follows [49]:

$$i_d = i_q = \sqrt{\frac{T_e}{\frac{3}{2} p(L_d - L_q)}} \quad (20)$$

By replacing the measured values by the reference values in Equation (20), we can write

$$i_d^* = i_q^* = \sqrt{\frac{T_e^*}{\frac{3}{2} p(L_d - L_q)}} \quad (21)$$

3.3. Optimal Currents Calculations

The electromagnetic torque of the machine can be written in the form [50]

$$T_e = \frac{1}{2} i^T \frac{\partial L}{\partial \theta} i \quad (22)$$

The currents in the $a - b - c$ frame can be written as the following:

$$i = \begin{bmatrix} i_a \\ i_b \\ i_c \end{bmatrix} = P(p\theta) \begin{bmatrix} i_d \\ i_q \\ i_h \end{bmatrix} = T_{32} \cdot R(\theta) \cdot \begin{bmatrix} i_d \\ i_q \end{bmatrix} \quad (23)$$

with

- i_h : zero sequence current assumed to be null;
- $P(p\theta)$: Park's matrix;
- $R(\theta)$: rotation matrix;

- T_{32} : Concordia matrix.

The machine torque can be written as:

$$T_e = \begin{bmatrix} i_d \\ i_q \end{bmatrix}^T \cdot R^T \cdot T_{32}^T \cdot \frac{\partial L(p\theta)}{\partial \theta} \cdot T_{32} \cdot R \begin{bmatrix} i_d \\ i_q \end{bmatrix} \quad (24)$$

We suppose

$$\begin{bmatrix} a(p\theta) & c(p\theta) \\ c(p\theta) & b(p\theta) \end{bmatrix} = R^T \cdot T_{32}^T \cdot \frac{\partial L(p\theta)}{\partial \theta} \cdot T_{32} \cdot R \quad (25)$$

By replacing (25) in (24), the torque is given as follows:

$$\Gamma_{em} = a(p\theta)i_d^2 + b(p\theta)i_q^2 + 2c(p\theta)i_di_q \quad (26)$$

The problem is to determine the currents i_d and i_q which will provide a constant torque. This problem has an infinite number of solutions. To remedy this, the solution which generates the least stator loss by joule effect is sought. The stator joule losses are defined by

$$P_j = R_s(i_d^2 + i_q^2) \quad (27)$$

The search for the solution becomes an optimization problem with the stator loss equation as an objective function of two variables and the torque Equation (27) as a constraint [51]:

$$\begin{cases} \Gamma_{em} = a(p\theta)i_d^2 + b(p\theta)i_q^2 + 2c(p\theta)i_di_q \\ (i_d^2 + i_q^2) \text{ to minimize} \end{cases} \quad (28)$$

In order to solve the problem, the Lagrangian function (Δ) is used. It can be written as

$$\Delta = (i_d^2 + i_q^2) + \mu \left(\Gamma_{em} - (a(p\theta)i_d^2 + b(p\theta)i_q^2 + 2c(p\theta)i_di_q) \right) \quad (29)$$

with μ being the Lagrange multiplier.

The derivation of Δ with respect to i_d , i_q , and μ gives

$$\begin{cases} 2i_q + \mu(-2ai_d - 2ci_q) = 0 \\ 2i_d + \mu(-2bi_q - 2ci_d) = 0 \\ T_e = a(p\theta)i_d^2 + b(p\theta)i_q^2 + 2c(p\theta)i_di_q \end{cases} \quad (30)$$

By solving the system of Equations (28), we can write

$$\begin{cases} i_q = \frac{(1-\mu a)i_d}{\mu c} \\ i_d = \sqrt{\frac{|T_e|}{\frac{\mu^2(a^2b-ac^2)+\mu(2c^2-2ab)+b}{\mu^2c^2}}} \end{cases} \quad (31)$$

$$\mu = \begin{cases} \frac{a+b+\sqrt{(a-b)^2+4c^2}}{2(ab-c^2)} & \text{if } T_e < 0 \\ \frac{a+b+\sqrt{(a-b)^2-4c^2}}{2(ab-c^2)} & \text{if } T_e > 0 \end{cases} \quad (32)$$

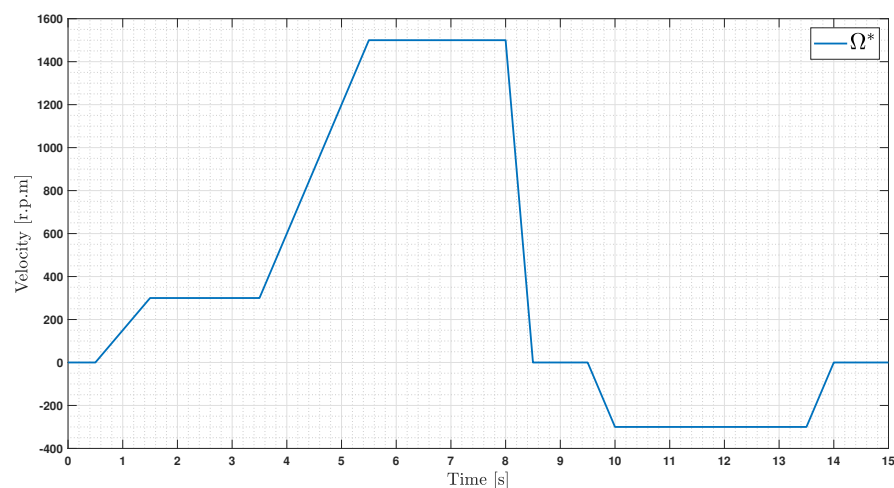
By replacing the measured values by the reference values in Equation (31), we can write

$$\begin{cases} i_q^* = \frac{(1-\mu a)i_d^*}{\mu c} \\ i_d^* = \sqrt{\frac{|T_e^*|}{\frac{\mu^2(a^2b-ac^2)+\mu(2c^2-2ab)+b}{\mu^2c^2}}} \end{cases} \quad (33)$$

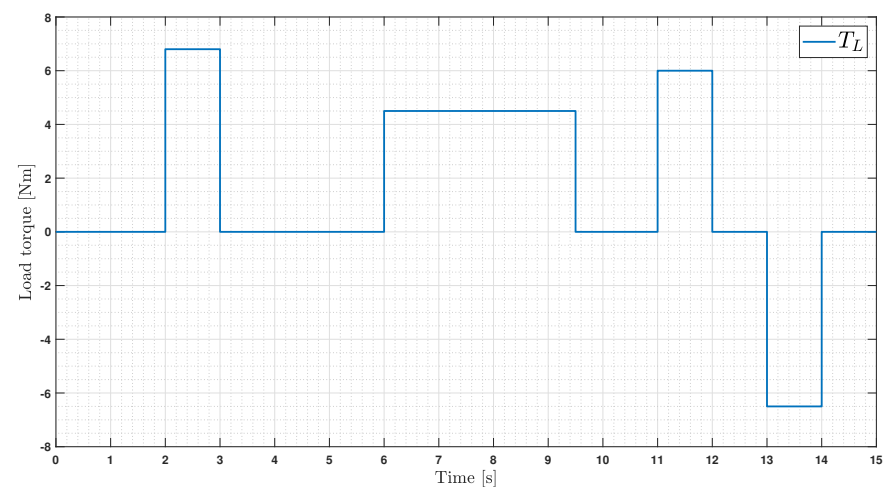
In this section, we are interested in the reduction in the torque ripple through the optimization of the reference current calculations used in the reference currents calculation bloc. In order to examine the developed method, the optimization of the reference currents are compared with the two methods of the literature, namely FOC and MTPA. For that, we will integrate the three methods in the reference currents calculation bloc in the cascade control strategy adopted in this study and presented in Section 2.2.

3.4. Simulation Results of Different Techniques of Current Calculation with PI Regulators

The reference currents calculation bloc will be used in this section to implement the three reference currents calculations that were previously described. A PI controller is used to regulate the velocity and current using the cascade velocity/currents control strategy. The simulation results were achieved using the Matlab/Simulink software tools, with the SynRM parameters utilized listed in Appendix A. The chosen velocity profile presented in Figure 5a covers multiple operating points: low velocity (300 rpm), nominal velocity (1500 rpm), and negative velocity (−300 rpm). As depicted in Figure 5b, various torque loads were applied at various points during the steady and transient states. The PI velocity controller parameters used are $K_p = 2.31$, $K_i = 387$, and PI currents controllers parameters used in the simulation are $K'_p = 1400$ and $K'_i = 10^6$.



(a)



(b)

Figure 5. Reference velocity and load torque profiles applied in the simulation: (a) reference velocity profile and (b) load torque profile.

3.4.1. Simulation with the Conventional Field-Oriented Control

The FOC reference currents calculation method is implemented in the reference currents calculation bloc as follows:

$$\begin{cases} i_d^* = 3 \text{ rated RMS current} \\ i_q^* = \frac{T_e^*}{p(L_d - L_q)i_d^*} \end{cases} \quad (34)$$

Figure 6 displays the velocity response using the conventional field-oriented control with respect to the selected profile. With no static error, the velocity closely matches the reference. Nevertheless, a tracking error results from the PI controller property. It is also important to note that the velocity has no overshoot thanks to the controllers' parameters chosen in the simulation.

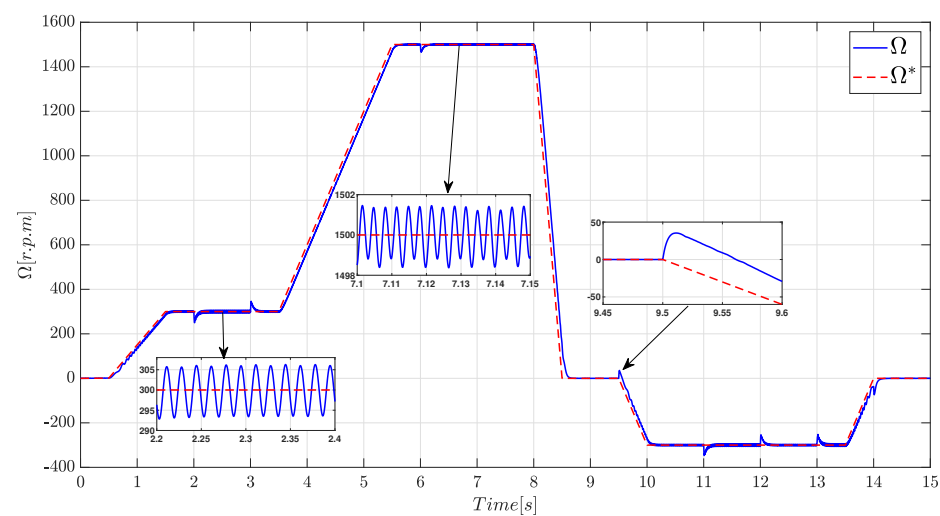


Figure 6. Velocity response obtained by PI controllers and conventional field-oriented control.

During the different moments of the application of the load torque, small decreases in machine velocity are observed compared to the reference. In the same way, small overshoots appear when the load is canceled. These drops and overshoots disappear gradually to return to the reference, as shown by the zooms in the figure.

For the current control, Figure 7 shows the evolution of the current components i_d and i_q . The evolution of the currents shows a good control of both current components over the different velocity and torque ranges, as shown in Figure 7a. Figure 7b demonstrates that even at low velocity the current is constant at the $i_d = 3A$ because of the value of $i_d^* = 3A$.

Although this method ensures the correct operation of the machine over the entire velocity/torque operating range, it can be seen that the reference current i_d^* is somewhat undulating, which has an impact on the current i_d and therefore on the torque ripple, as shown in the different zooms of Figure 7a.

The torque evolution is shown in Figure 8. In this strategy, the torque has been controlled from the calculation of the reference current using the classical field-oriented control. It can be seen that the torque is able to convince the load torque (T_L) and the intrinsic torque of the machine ($f_r\Omega$). Nevertheless, as illustrated in the zooms in Figure 8, this technique results in significant machine torque ripples at low and high machine velocities, which are quantified at 41.07 and 48.08% with the torque load, respectively.

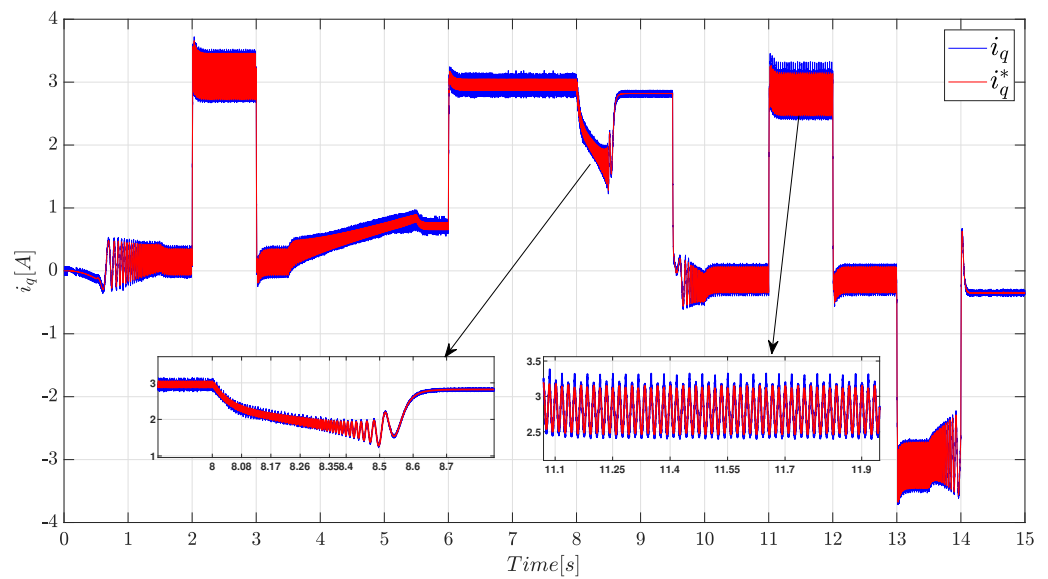
The torque ripple rate is calculated at a steady state as follows:

$$\Delta T_e(\%) = \frac{T_{e_{max}} - T_{e_{min}}}{T_{e_{avg}}} \times 100 \quad (35)$$

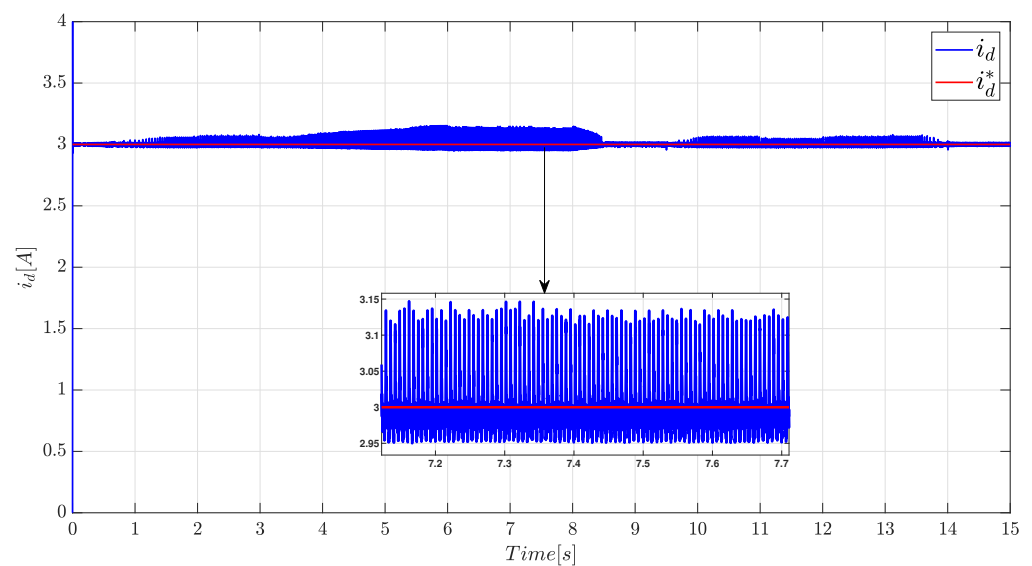
- $T_{e_{max}}$: the maximum torque value.
- $T_{e_{min}}$: the minimum torque value.
- $T_{e_{avg}}$: the average torque value.

These ripples are caused by the control of stator currents, which are directly related to torque, as given in Equation (12). In other words, the conventional field-oriented control does not provide optimal reference currents for optimizing stator currents and, as a result, the reduction in torque ripples.

In the following part, the maximum torque per ampere (MTPA) method is tested under the same simulation conditions to determine its capacity to reduce the machine's torque ripple.



(a)



(b)

Figure 7. Response of the current components obtained by the PI controllers and the conventional field-oriented control: (a) i_q response and (b) i_d response.

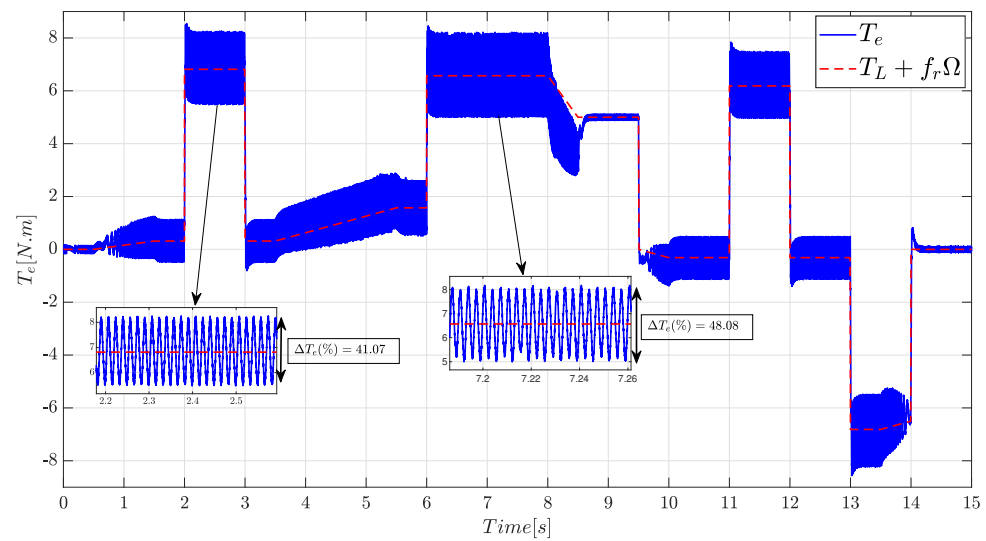


Figure 8. Torque response obtained by PI controllers and conventional field-oriented control.

3.4.2. Simulation with the Maximum Torque per Ampere Method

Applying the same simulated conditions as in the previous section. Similarly, the MTPA approach will be implemented in the reference currents calculation bloc as follows:

$$i_d^* = i_q^* = \sqrt{\frac{T_e^*}{\frac{3}{2}p(L_d - L_q)}} \quad (36)$$

Figure 9 depicts the velocity response to the profile selected using the maximum torque per ampere approach. The velocity closely follows the reference with no static error. However, there is a tracking error caused by the PI regulator's property. It should also be observed that the velocity has no overshoot. This is due to the regulator parameters chosen.

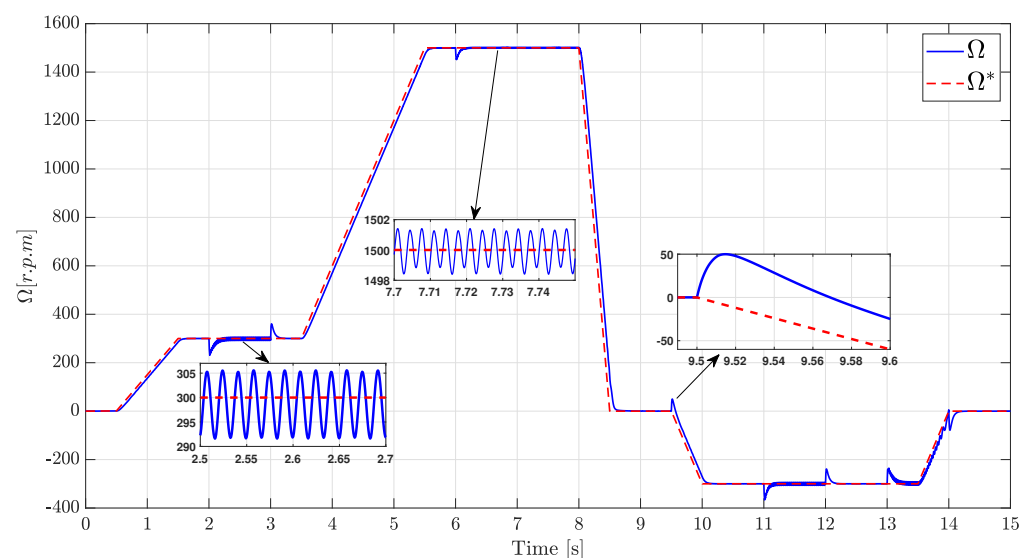
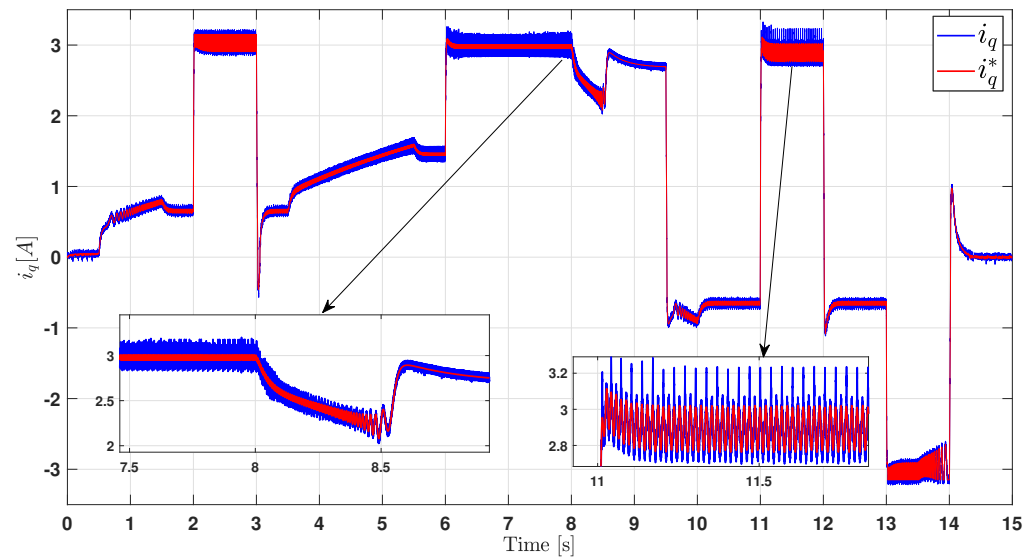


Figure 9. Velocity response obtained by PI controllers and maximum torque per ampere method.

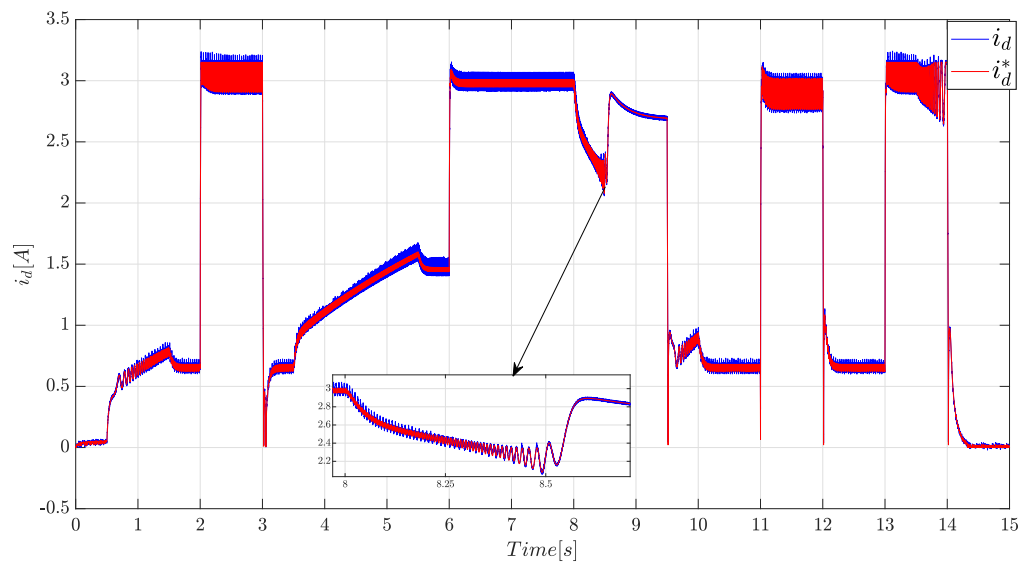
Figure 10 illustrates the evolution of the current components i_d and i_q for current regulation. The evolution of the currents also shows a satisfactory regulation of the two current components over a wide range of velocity and torque. Similarly, the zooms in Figure 10a,b show that the reference currents exhibit undulations that affect the stator currents and therefore the torque ripple.

Figure 11 shows the machine's torque. From this illustration, we can see that the maximum torque per ampere method provides a machine torque that can overcome the load torque (T_L) and the intrinsic torque ($f_r\Omega$) of the machine. Although the torque ripple rate is a bit lower compared to the FOC method, the machine's torque still contains a significant ripple. The torque ripple rates at low and high machine velocities are quantified at 47.07 and 47.02% with the torque load, respectively, as illustrated in the zooms in Figure 11.

In the following section, we will put the optimal currents calculations method to the test under identical simulation conditions in order to evaluate whether it can reduce the machine's torque ripple.



(a)



(b)

Figure 10. Response of the current components obtained by the PI controllers and the maximum torque per ampere method: (a) i_q response and (b) i_d response.

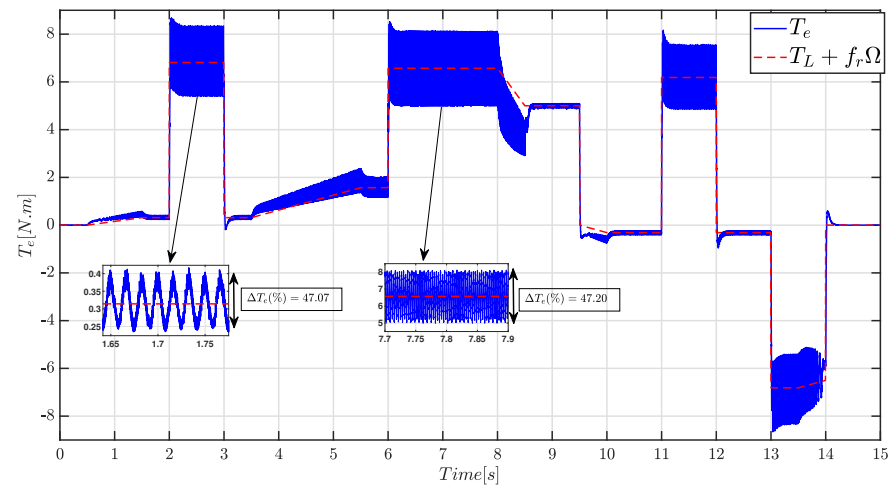


Figure 11. Torque response obtained by PI controllers and maximum torque per ampere method.

3.4.3. Simulation with the Optimal Currents Calculations Method (OCCM)

The same simulated conditions used for FOC and MTPA is also implemented for the optimal currents calculation method (OCCM). Similarly, in the reference currents calculation bloc, the optimal currents calculations method (OCCM) will be implemented as follows:

$$\begin{cases} i_q^* = \frac{(1-\mu a)i_d}{\mu c} \\ i_d^* = \sqrt{\frac{|T_e^*|}{\frac{\mu^2(a^2b-ac^2)+\mu(2c^2-2ab)+b}{\mu^2c^2}}} \end{cases} \quad (37)$$

Figure 12 shows the velocity response of the system for the selected profile. The velocity onset has the same dynamic characteristics as in the previous case. However, the velocity fluctuations are very small compared to the previous case.

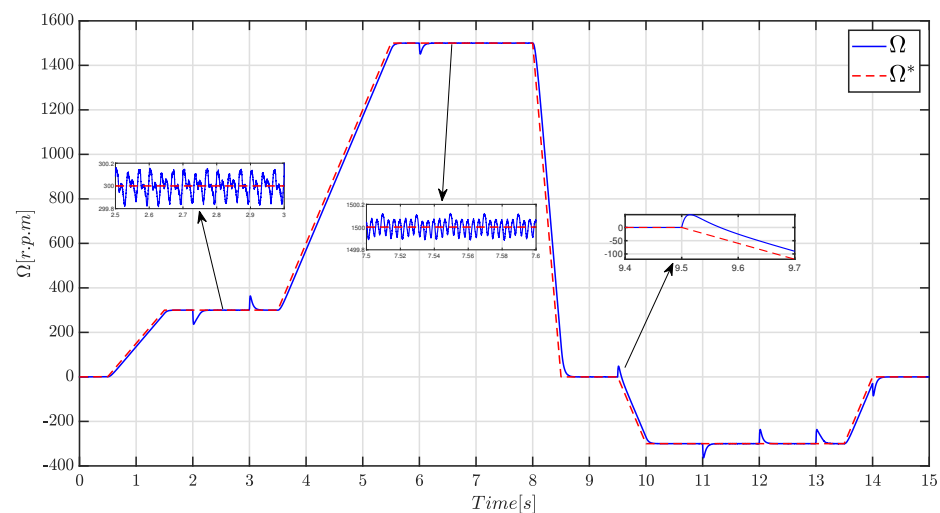


Figure 12. Velocity response obtained by PI controllers and optimal currents calculations method.

Figure 13 shows a good control of the current components i_d and i_q . The current components show a reduction in fluctuations, as shown by the zooms in Figure 13a,b. This can be justified by optimizing the reference currents, which necessarily has an impact on minimizing the torque ripple of the machine.

Figure 14 shows the machine's torque. The optimal currents calculations method as shown in Figure 14 assures a machine torque that can convince the machine's load torque (TL) and intrinsic torque ($f_r\Omega$). Moreover, there is a minimization of the machine torque ripple 9.08 and 10.8% with the torque load. This can be justified by the optimization in the reference currents; therefore, the optimization in the currents regulation impacts on the minimization of the torque ripple.

The different reference current calculation strategies presented similar dynamic performances of the currents and velocity control. However, the optimization of the reference current can reduce the torque ripple of the machine. The optimum current method solves the problem of excessive consumption and minimizes torque ripples over the entire operating range. The minimization is performed with a harmonized stator current.

Table 1 summarizes the torque ripple rate for the three examined methods.

Table 1. Comparison of torque ripple rates of the three strategies

	FOC		MTPA		OCCM	
ΔT_e	Without Load	With Load	Without Load	With Load	Without Load	With Load
At 300 r.p.m	383%	41.7%	50%	40.7%	38.08%	9.08%
At 1500 r.p.m	130%	48.8%	53.7%	47.2%	17.3%	10.8%

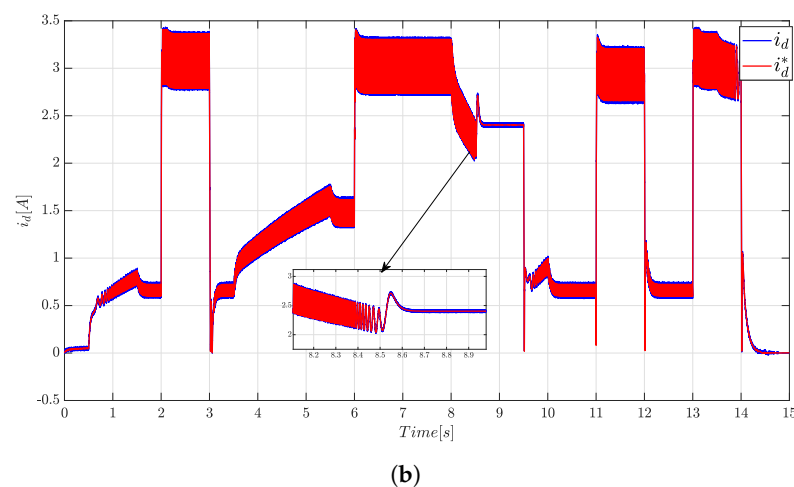
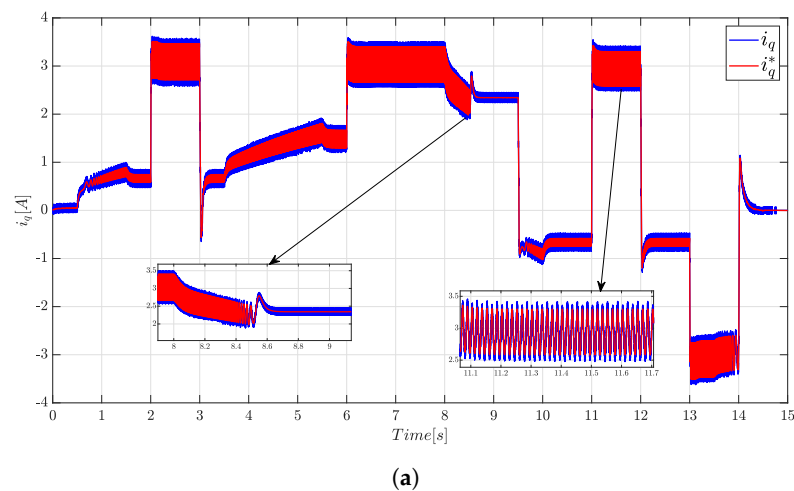


Figure 13. Response of the current components obtained by the PI controllers and optimal currents calculations method: (a) i_q response and (b) i_d response.

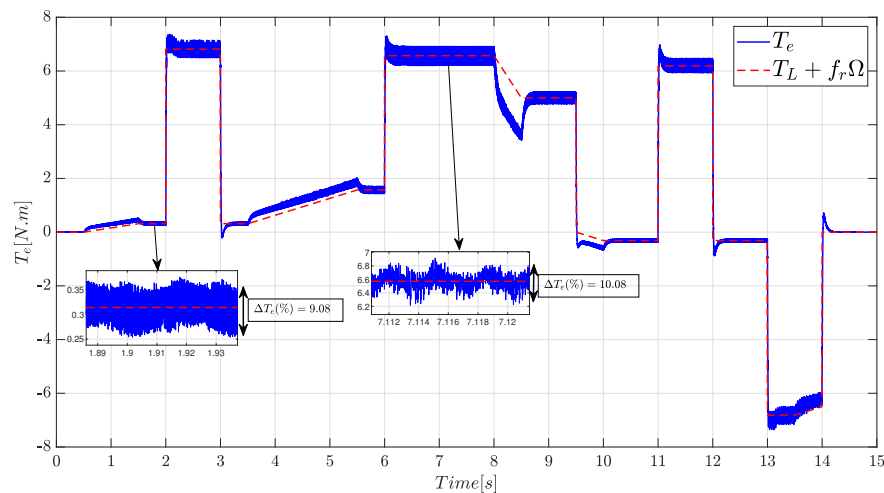


Figure 14. Torque response obtained by PI controllers and optimal currents calculations method.

4. Torque Ripple Minimization by Using Advanced Control Techniques

The reference currents calculation bloc can be used to minimize the machine torque ripple, as we have observed in this study. The optimal current calculation method (OCCM), when compared to the FOC and MTPA methods, was proven to be effective at reducing the torque ripple of the synchronous reluctance machine.

In this part, the torque ripple is reduced by using advanced controls. Indeed, the torque is directly linked to the stator currents of the machine. Therefore, better control of these currents can impact the torque ripple. Our objective is to investigate this hypothesis by improving the control of the currents with advanced controls based on the theory of sliding mode control in order to improve the dynamic performance (suppression of the tracking error) and robustness. The optimal current calculation method will be combined with the sliding mode control that replaces the PI velocity and currents controllers.

A conventional sliding mode control (SMC) is proposed to replace the PI controllers. However, due to the disadvantages of the control, particularly the chattering phenomenon [52], a second-order sliding mode control based on a super-twisting algorithm (STA) to minimize the chattering and improve the current response, and thereby reducing the torque ripple, is proposed.

4.1. Sliding Mode Control

Sliding mode control (SMC) is a class of a variable structure system (VSS) that targets decreasing the complexity of high-order systems to first-order state variables, defined as a sliding function and its derivative [53]. It is characterized by its simplicity of implementation, very good dynamic responsiveness, and, most importantly, its robustness with respect to internal uncertainties, as manifested by an insensitivity to variations in the parameters of the system to be controlled, as well as external disruptions [54–56].

This section will synthesize a conventional sliding mode control for velocity and currents control to replace PI controllers in the velocity/currents cascade control strategy.

4.1.1. Synthesis of a Conventional Sliding Mode for Velocity Controller

The selected sliding surface depends on the velocity tracking error (e_Ω) as follows:

$$e_\Omega(t) = \Omega^*(t) - \Omega(t) \quad (38)$$

The expression of the sliding surface (s_1) is

$$s_1(t) = e_\Omega(t) + \lambda_1 \int_0^t e_\Omega(\tau) d\tau \quad (39)$$

where λ_1 is a positive constant ($\lambda_1 > 0$).

This choice of sliding surface results in an error that tends to zero (if $s_1 = 0$, then $e_\Omega = 0$).

Thus, the following state variables are used:

$$\begin{cases} x_1(t) = \int_0^t e_\Omega(\tau) d\tau \\ x_2(t) = e_\Omega(t) \end{cases} \quad (40)$$

With x_1 and x_2 representing, respectively, the error and its integral. From (40), we deduce that

$$\dot{x}_1(t) = x_2(t) \quad (41)$$

Thus, the sliding surface can be defined as

$$s_1(t) = x_2(t) + \lambda_1 x_1(t) \quad (42)$$

Therefore, the electromechanical Equation (7) of the SynRM model is rewritten as follows:

$$\begin{aligned} \dot{x}_2 &= \dot{\Omega}^* - \frac{1}{J} T_e + \frac{f_r}{J} \Omega + \frac{1}{J} T_L \\ &= \dot{\Omega}^* - \frac{1}{J} T_e + \frac{f_r}{J} (\Omega - \Omega^* + \Omega^*) + \frac{1}{J} T_L \\ &= \dot{\Omega}^* - \frac{1}{J} T_e + \frac{f_r}{J} \Omega^* - \frac{f_r}{J} x_2 + \frac{1}{J} T_L \end{aligned} \quad (43)$$

Then, the system can be put in the form of a state space representation:

$$\begin{cases} \dot{x}_1 = x_2 \\ \dot{x}_2 = f(x) + gu + d \end{cases} \quad (44)$$

With $f(x) = \dot{\Omega}^* + \frac{f_r}{J} \Omega^* - \frac{f_r}{J} x_2$, $g = \frac{1}{J}$, $u = T_e$, $d = \frac{1}{J} T_L$.

In order to determine the continuous component (u_c) of the SMC [57,58],

$$\dot{s}_1(x) = s(x) = 0 \quad (45)$$

Thus, considering (42) and (44), assuming that $u = u_c$,

$$u_c = g^{-1}(-f(x) - d - \lambda_1 x_2) \quad (46)$$

The existence and convergence condition [58] is used to determine the discontinuous component (u_d) as follows:

$$s_1(x) \cdot \dot{s}_1(x) < 0 \quad (47)$$

Given that,

$$\dot{s}_1(x) = \dot{x}_2(t) + \lambda_1 \dot{x}_1(t) \quad (48)$$

After simplification and by posing $u = u_d$,

$$u_d = -c_1 \text{sign}(s_1) \quad (49)$$

Knowing that the sliding mode control law is the sum of the continuous control and the discontinuous components [58],

$$u = u_{eq} + u_d \quad (50)$$

By replacing (46) and (49) in (50),

$$u = J\dot{\Omega}^* + f_r\Omega^* + (\lambda_1 J - f_r)e_\Omega + T_L - c_1 \text{sign}(s_1) \quad (51)$$

where the control u represents the total reference torque T_e^* provided by the velocity controller. The term T_L is considered as a disturbance to be compensated by the controller. The final sliding mode control law for velocity is

$$T_e^* = J\dot{\Omega}^* + f_r\Omega^* + (\lambda_1 J - f_r)e_\Omega - c_1 \text{sign}(s_1) \quad (52)$$

4.1.2. Synthesis of a Conventional Sliding Mode for Currents Controllers

The same method of synthesizing the velocity control law is used for the two current components i_d and i_q . Similarly, the sliding surfaces (s_2 and s_3) are defined in terms of the current tracking error (e_d and e_q) as follows:

$$\begin{cases} s_2(t) = e_d(t) + \lambda_2 \int_0^t e_d(\tau) d\tau \\ s_3(t) = e_q(t) + \lambda_3 \int_0^t e_q(\tau) d\tau \end{cases} \quad (53)$$

where λ_2 and λ_3 are positive constants.

The electrical Equation (3) can be rewritten in the following form:

$$\begin{cases} \frac{di_d}{dt} = v_d - \frac{L_d}{R_s} i_d + pL_q \Omega i_q \\ \frac{di_q}{dt} = v_q - \frac{L_q}{R_s} i_q - pL_d \Omega i_d \end{cases} \quad (54)$$

The terms $pL_q \Omega i_q$ and $pL_d \Omega i_d$ are considered as disturbances to be compensated by the current regulators. Thus, (54) becomes

$$\begin{cases} \frac{di_d}{dt} = v_d - \frac{L_d}{R_s} i_d \\ \frac{di_q}{dt} = v_q - \frac{L_q}{R_s} i_q \end{cases} \quad (55)$$

In the same way as the SMC velocity controller, to find the continuous components, the following condition is used:

$$\begin{cases} \dot{s}_2(x) = s_2(x) = 0 \\ \dot{s}_3(x) = s_3(x) = 0 \end{cases} \quad (56)$$

Thus, the continuous components (v_{cd} and v_{cq}) have the following form:

$$\begin{cases} v_{cd} = L_d \frac{di_d^*}{dt} + R_s i_d^* + (\lambda_1 L_d - R_s) e_{i_d} \\ v_{cw} = L_q \frac{di_q^*}{dt} + R_s i_q^* + (\lambda_1 L_q - R_s) e_{i_q} \end{cases} \quad (57)$$

In order to determine the discontinuous components, the convergence condition is used as follows:

$$\begin{cases} \dot{s}_2(x) < s_2(x) = 0 \\ \dot{s}_3(x) < s_3(x) = 0 \end{cases} \quad (58)$$

After simplification, the discontinuous components (v_{d_d} and v_{d_q}) are written as

$$\begin{cases} v_{d_d} = -c_2 \text{sign}(s_2) \\ v_{d_q} = -c_3 \text{sign}(s_3) \end{cases} \quad (59)$$

The sliding mode control law for the i_d and i_q currents controllers is the sum of the continuous and discontinuous components:

$$\begin{cases} u_d = v_{d_c} + v_{d_d} \\ u_q = v_{q_c} + v_{q_d} \end{cases} \quad (60)$$

where u_d and u_q represent the voltages generated by SMC i_d and i_q currents controllers. Finally, the conventional sliding mode control law of the currents i_d and i_q can be written as

$$\begin{cases} v_d = v_{d_c} + v_{d_d} \\ v_q = v_{q_c} + v_{q_d} \end{cases} \quad (61)$$

4.1.3. Simulation Results

In this section, the conventional sliding mode controllers developed in the cascade control strategy (see Section 2.2) are implemented using the optimal current calculation method (OCCM). To evaluate the conventional SMC against the PI controllers, the same torque and velocity profiles presented in Section 3.4 were used. The controller parameters used are $\lambda_1 = 3$, $c_1 = 1$, $\lambda_2 = \lambda_3 = 2$, and $c_2 = c_3 = 5$.

Figure 15 shows a very good response over the entire velocity and torque range. In contrast to the PI control (see Figure 12), the static error and tracking error are almost zero. It should also be noted that the velocity fluctuations are very small or even negligible. The velocity drops and overshoots when applying or removing the load have been significantly reduced, as shown by the zooms in Figure 15.

From this result, the static and dynamic performance of the velocity response is significantly improved by using an SMC velocity controller.

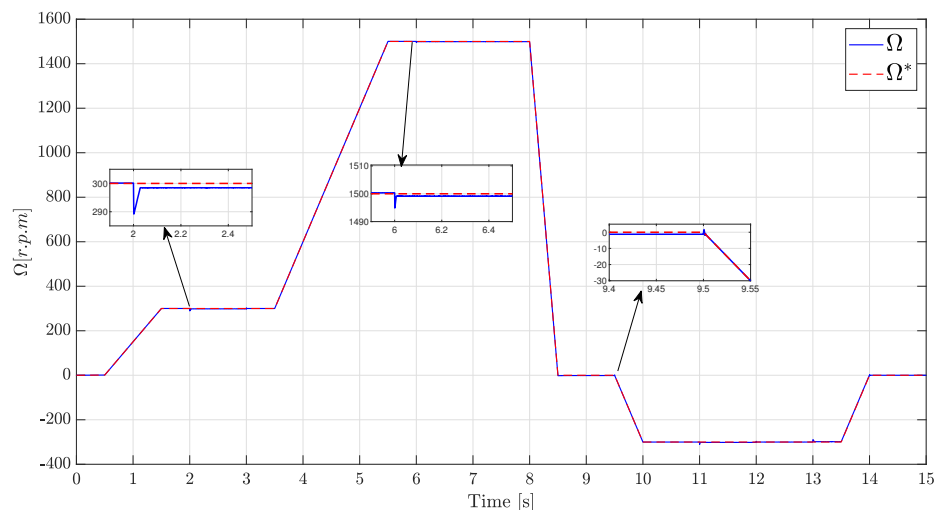


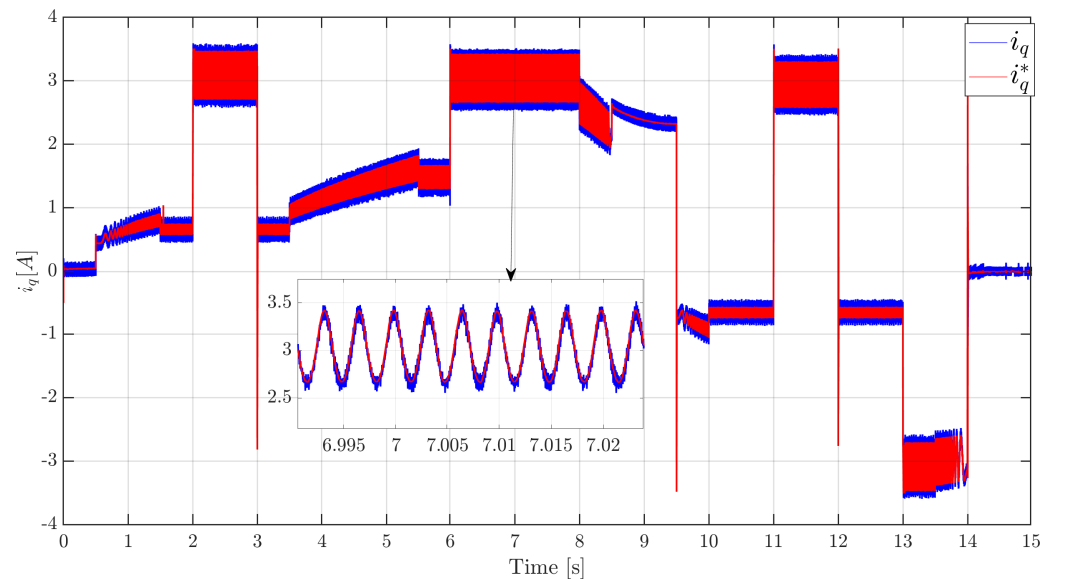
Figure 15. Velocity response obtained by SMC controller and optimal currents calculations method.

For the currents control, Figure 16 shows good control of the i_d and i_q current components. The current curve shows large current peaks compared to the PI controller (see Figure 13). These peaks are due to the high dynamics of the velocity controller to eliminate the tracking error. Moreover, it is caused by the discontinuous theme of the SMC or, as it is called in the literature, the chattering phenomenon.

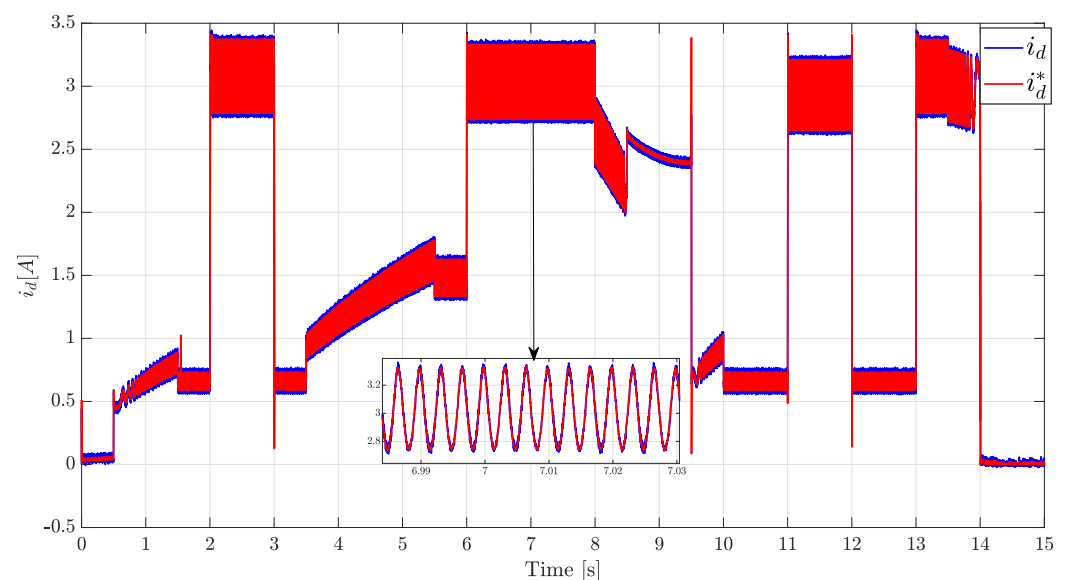
The torque response of the SynRM employing the SMC is shown in Figure 17. It can be seen from this figure that the SMC with the optimal current calculation method ensures a machine torque that can convince the resistive torque (T_L) and the intrinsic torque ($f_r\Omega$) of the machine.

When compared to the PI controllers, at a very low speed and under load, for example, the torque response in the sliding mode shows a slight increase in torque ripples (10.07% compared to PI 9.8%). These ripples are a consequence of the chattering effect which is a drawback of the sliding mode control.

The next section suggests a control strategy based on the theory of higher-order sliding mode control to address this flaw.



(a)



(b)

Figure 16. Response of the current components obtained by the SMC controllers and optimal currents calculations method: (a) i_q response and (b) i_d response.

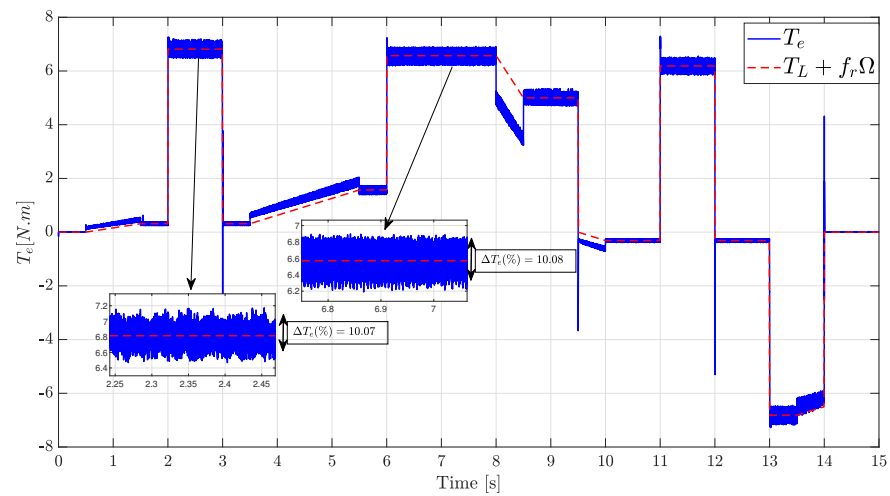


Figure 17. Torque response obtained by SMC controllers and optimal currents calculations method.

4.2. Higher-Order Sliding Mode Control

The control of systems by the classical sliding mode has shown that it presents an undesirable chattering phenomenon. In order to reduce or eliminate these phenomena, many solutions have been proposed in the literature [59].

The higher-order sliding mode has been chosen, and this method is based on the theory of the classical sliding mode control presented previously. In addition, it ensures that the desired performance is maintained and that there is a better convergence accuracy. The discontinuous control term is applied to the higher-order derivatives of the sliding variable while maintaining the advantages of the classical sliding mode control, because the discontinuity does not appear directly in the control but rather in one of its higher derivatives [59,60].

To lessen the chattering phenomenon, we suggest using a second-order sliding mode control built on the super-twisting algorithm (STA) in this work. By minimizing this phenomenon, the excellent static and dynamic performances offered by the conventional sliding mode control are maintained while reducing the torque ripple. In order to determine its effect on the torque ripple of the synchronous reluctant machine, we will thus propose the STA for the velocity and currents controllers and evaluate it against the SMC and the PI.

4.2.1. Synthesis of the Velocity Controller by Super-Twisting Algorithm

For the synthesis of the speed controller, the sliding surface s_4 is defined by

$$s_4(t) = y_1(t) = e_\Omega(t) + \lambda_1 \int_0^t e_\Omega(\tau) d\tau \quad (62)$$

This sliding surface is chosen similarly to that of the conventional sliding mode control. From the mechanical Equation (7) of the SynRM,

$$\dot{\Omega} = \frac{1}{J} T_e - \frac{f}{J} \Omega - \frac{1}{J} T_L \quad (63)$$

Using (62) and (63), the derivative of the surface is expressed as

$$\dot{\Omega} = \frac{1}{J} T_e - \frac{f}{J} \Omega - \frac{1}{J} T_L \quad (64)$$

It should be noted that the super-twisting algorithm system is specifically developed for systems with a relative degree $n = 1$ whose goal is to reduce chattering problems. This algorithm does not require the knowledge of the second derivative of the sliding variable as in the case of other algorithms. Thus, the algorithm guarantees that the trajectories of

the system twist around the origin in the phase portrait [61] which brings about having the model of the system in relative order one:

$$\dot{y}_1 = \phi(y_1, t) + Y(x, t)u_{ST}(t) \quad (65)$$

with y_1 being the sliding surface, and ϕ and Y being bounded functions [62,63]:

$$\begin{cases} |\phi| \leq \Phi \\ 0 < Y_m \leq Y(x, t) \leq Y_M \end{cases} \quad (66)$$

From Equations (65) and (64), we can deduce

$$\dot{y}_1 = \dot{\Omega}^* + \frac{f}{J}\Omega^* + \left(\frac{-f_r}{J} + \lambda_1\right)e_\Omega + \frac{1}{J}T_L - \frac{1}{J}T_e \quad (67)$$

The definition of the upper and lower bounds of the previously defined functions is chosen as follows [47]:

$$\begin{cases} \phi_{ST} = \dot{\Omega}^* + \frac{f}{J}\Omega^* + \left(\frac{-f}{J} + \lambda_1\right)e_\Omega + \frac{1}{J}T_L \\ Y_{ST} = 1 \\ u_{ST} = -\frac{1}{J}T_e \end{cases} \quad (68)$$

So, the sufficient conditions of convergence can be chosen as

$$\begin{cases} W = 3\Phi_{ST} \\ \lambda = 5\sqrt{2\Phi_{ST}} \\ \rho = 0.5 \end{cases} \quad (69)$$

By choosing $S_0 = s_4^2$, the order can be written as

$$u_{ST} = u_1 + u_2 \quad (70)$$

With

$$\begin{cases} \dot{u}_1 = -W\text{sign}(s_1) \\ \dot{u}_2 = -\lambda|s_1|^{0.5}\text{sign}(s_1) \end{cases} \quad (71)$$

4.2.2. Synthesis of Current Controllers by Super-Twisting Algorithm

In a similar way to the surface used in the classical sliding mode, the sliding surfaces of the currents (s_5 and s_6) are defined by

$$\begin{cases} s_5(t) = y_2(t) = e_d(t) + \lambda_2 \int_0^t e_d(\tau) d\tau \\ s_6(t) = y_3(t) = e_q(t) + \lambda_3 \int_0^t e_q(\tau) d\tau \end{cases} \quad (72)$$

From the electrical equations of the machine, the surface derivatives can be expressed as

$$\begin{cases} \dot{y}_2 = \dot{i}_d^* + \frac{R}{L_d}i_d^* + \left(\frac{-R}{L_d} + \lambda_1\right)e_d + \frac{1}{L_d}E_q - \frac{1}{L_d}v_d \\ \dot{y}_3 = \dot{i}_q^* + \frac{R}{L_q}i_q^* + \left(\frac{-R}{L_q} + \lambda_1\right)e_q + \frac{1}{L_q}E_d - \frac{1}{L_q}v_q \end{cases} \quad (73)$$

From Equations (65) and (73), we can deduce

$$\begin{cases} \phi_{d_{ST}} = i_d^* + \frac{R}{L_d} \Omega^* + \left(\frac{-R}{L_d} + \lambda_1 \right) e_d + \frac{1}{L_d} E_q \\ Y_{d_{ST}} = 1 \\ u_{d_{ST}} = -\frac{1}{L_d} v_d \end{cases} \quad \begin{cases} \phi_{q_{ST}} = i_q^* + \frac{R}{L_q} i_q^* + \left(\frac{-R}{L_q} + \lambda_1 \right) e_q + \frac{1}{L_q} E_d \\ Y_{q_{ST}} = 1 \\ u_{q_{ST}} = -\frac{1}{L_q} v_q \end{cases} \quad (74)$$

The upper and lower bounds of the previously defined functions are chosen as follows:

$$\begin{cases} \Phi_{d_{ST}} = \left| i_d^* + \frac{R}{L_d} i_d^* + \left(\frac{-R}{L_d} + \lambda_1 \right) e_d \right| + \left| \frac{1}{L_d} E_q \right| \\ Y_{d_{mST}} = 0.5, Y_{d_{MST}} = 1 \\ U_d = -\frac{1}{L_d} v_{d_{max}} \end{cases} \quad \begin{cases} \Phi_{q_{ST}} = \left| i_q^* + \frac{R}{L_q} i_q^* + \left(\frac{-R}{L_q} + \lambda_1 \right) e_q \right| + \left| \frac{1}{L_q} E_d \right| \\ Y_{q_{mST}} = 0.5, Y_{q_{MST}} = 1 \\ U_q = -\frac{1}{L_q} v_{q_{max}} \end{cases} \quad (75)$$

4.2.3. Simulation Results

Using the OCCM reference currents calculation bloc with the identical velocity and torque profile in the PI and SMC case, the STA sliding mode controllers of the velocity and currents were implemented in the cascade control strategy.

Figure 18 demonstrates excellent tracking over the whole velocity range. A zero static error and zero tracking error are displayed in the velocity response. Overshoot and undershoot are extremely rare, and there are barely any velocity fluctuations, as shown in the zooms of the figure.

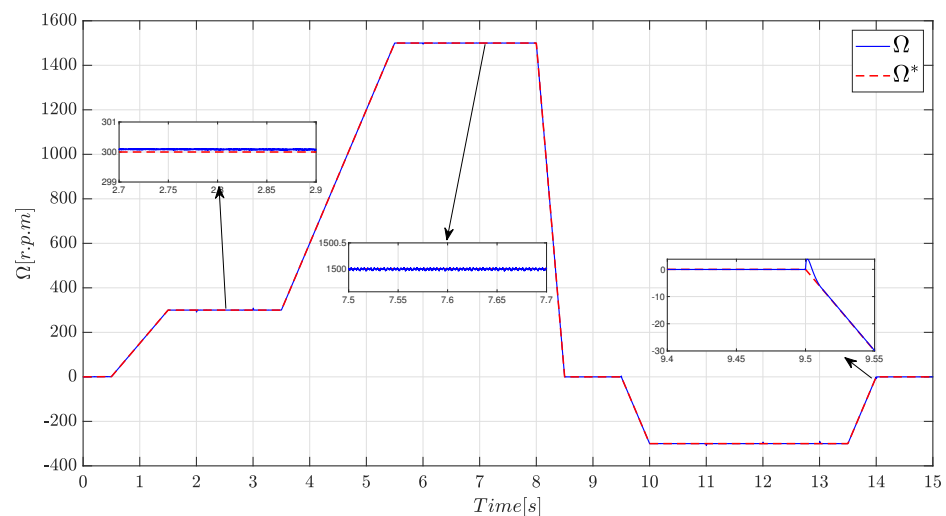


Figure 18. Velocity response obtained by STA controller and optimal currents calculations method.

Figure 19 shows good regulation of the current components i_d and i_q . The waveform of the currents is similar to the SMC case with less fluctuation, as shown in the zooms.

Figure 20 depicts the torque response of the SynRM using the SMC. It shows that the SMC with the optimal current calculation method assures a machine torque that can convince the machine's load torque (T_L) and intrinsic torque ($f_r \Omega$). When compared to the PI and SMC control, the torque response of the STA control demonstrates a reduction in the torque ripple. As an illustration, at a low speed with load, the torque ripple rate in the PI control is 9.8%, 10.07% in the SMC control, and 5% in the STA control.

Table 2 summarizes the machine torque ripple rate for low and high speeds with and without load torque.

Table 2. Comparison of torque ripple rates for the three control modes.

	PI		SMC		STA	
ΔT_e	Without Load	With Load	Without Load	With Load	Without Load	With Load
At 300 r.p.m	38.08%	9.8%	43%	10.07%	29%	5%
At 1500 r.p.m	17.3%	10.8%	21.7%	10.8%	12.7%	8%

This table makes it abundantly evident that applying STA control considerably reduces the torque ripple of the synchronous reluctance machine.

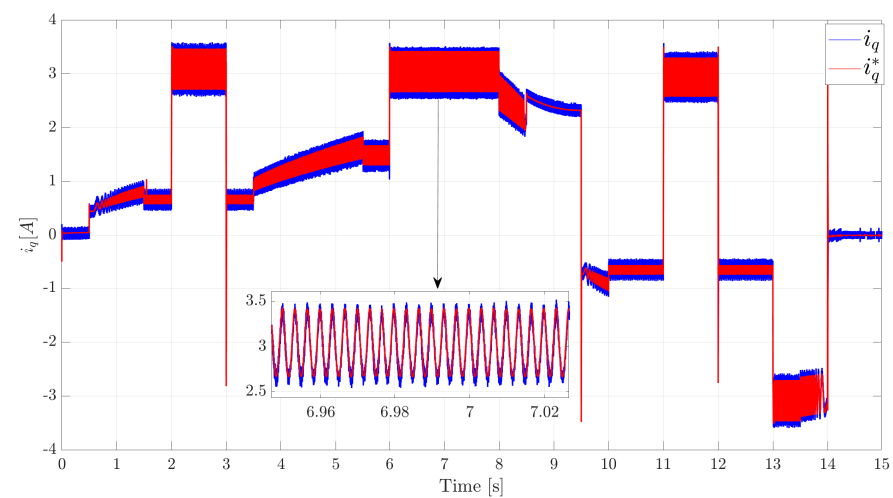
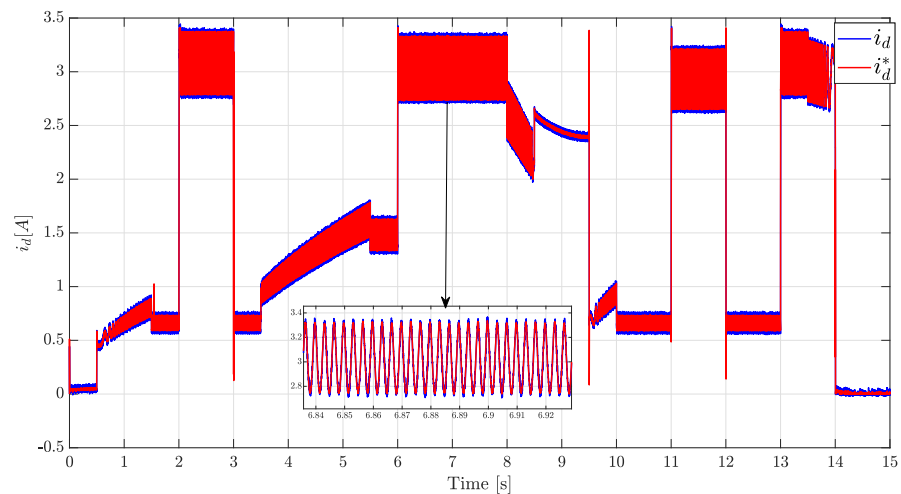
**(a)****(b)**

Figure 19. Response of the current components obtained by the STA controllers and optimal currents calculations method: **(a)** i_q response and **(b)** i_d response.

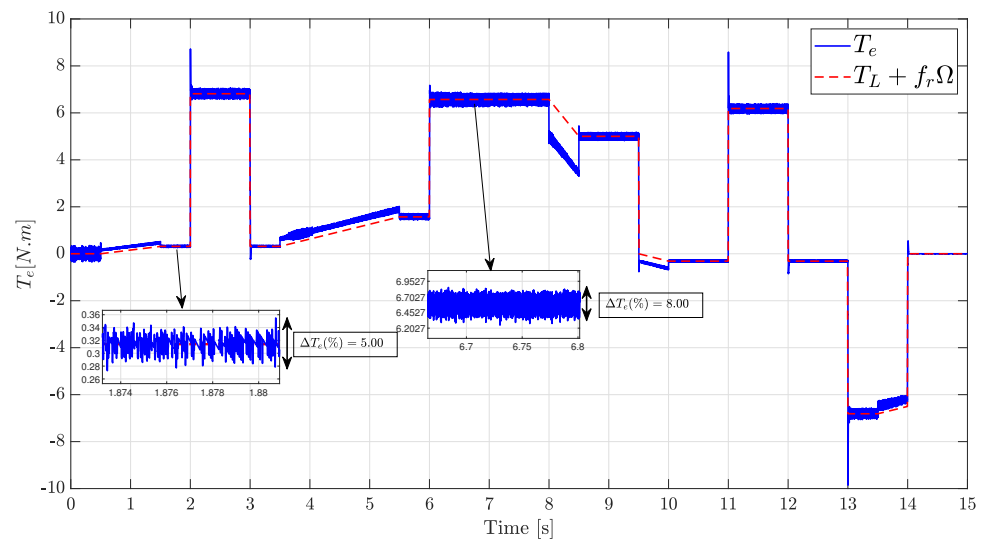


Figure 20. Torque response obtained by STA controllers and optimal currents calculations method.

5. Conclusions

In this work, we addressed the problem of torque ripple reduction in a synchronous reluctance machine for an electric vehicle drivetrain application.

We have based our approach on control-based solutions. In a cascade velocity/currents control strategy, we first proposed a new reference currents calculation bloc based on the optimization of the stator joule loss. In order to examine the contribution of this method on torque ripple reduction, we compared it to two methods used in the literature, namely the conventional field-oriented control and maximum torque per ampere. The simulation results clearly show the effectiveness and superiority of this proposed method in reducing the torque ripple of the machine.

To improve the system's static and dynamic performance, in the second part, we synthesized advanced velocity and current controllers based on the variable structure theory. Classical sliding mode controllers have been proposed using the method provided in the first part, namely the calculation of optimal currents. When compared to the PI controllers, the simulation results demonstrate a gain in performance but a minor increase in torque ripple. This is related to the chattering phenomenon, which constitutes the drawback of conventional sliding mode control. We then presented second-order sliding mode controllers based on the super-twisting algorithm to avoid this problem. The simulation results show that in addition to the improvement in the drivetrain performance, the torque ripples are significantly reduced.

In conclusion, a combination of the optimal current calculation method and the second-order sliding mode control produces the most effective combination for improving the synchronous reluctance machine's performance and torque ripple reduction.

Author Contributions: Methodology, O.D.A., M.O., Y.S., T.M., M.B. and K.H.A.; Software, O.D.A., M.O. and Y.S.; Validation, O.D.A., M.B. and Y.S.; Formal analysis, Y.S., T.M. and M.B.; Data curation, Y.S.; Writing—original draft, O.D.A. and Y.S.; Writing—review & editing, M.B. and Y.S.; Visualization, Y.S. and M.B.; Supervision, Y.S. and M.B. All authors have read and agreed to the published version of the manuscript.

Funding: This research received no external funding

Conflicts of Interest: The authors declare no conflict of interest.

Abbreviations

The following abbreviations are used in this manuscript:

EV	Electric vehicle
SynRM	Synchronous reluctance machines
PMSM	Permanent magnet synchronous machine
WRSM	Wound rotor synchronous machine
REMs	Rare-earth materials
FOC	Field-oriented control
DFOC	Direct field-oriented control
ILOC	Indirect field-oriented control
MTPA	Maximum torque per ampere
OCCM	Optimum current calculation method
PI	Proportional integral
SMC	Sliding mode control
STA	Super-twisting algorithm
$\phi_s, \phi_{ds}, \phi_{qs}$	Stator flux linkage in the d and q axes
i_d, i_q	Stator current in the d and q axes
V_d, V_q	Voltages in the d and q axes
L_{ds}, L_{qs}	Inductance in the d and q axes
L_i	Stator inductance of phase i
M_{ij}	Mutual inductance between phases i and j
Ω	Rotational velocity of the machine, in rad/s.
Ω^*	Rotational velocity reference of the machine, in rad/s.
T_e	Electromagnetic torque produced by the machine, in Nm
T_L	Load torque, in Nm
f_r	Viscous friction coefficient, in Ns^2/m^2
F_m	The slope force or tractive force that is required to drive the vehicle up
f_{aero}	Aerodynamic force created by the friction of the vehicle's body moving through the air
F_{rr}	Rolling resistance force
F_{rc}	Resistance force exerted by the vehicle weight as it goes up and down a hill
M	Vehicle mass
g	The acceleration due to gravity on Earth
ρ	Density of the air, in kg/m^3
C_x	Drag coefficient
S_f	Frontal cross-sectional area, in m^2
R_{sc}	Rolling resistance opposing the slope
i_d^*, i_q^*	Reference current in the d and q axis
Δ	Lagrangian function used to optimize the currents

Appendix A

Table A1. The synchronous reluctance machine's parameters.

Parameter	Value
Rated power	$P_n = 1.1 \text{ kW}$
Number of pole pairs	$p = 2$
Rated RMS current	$I = 3 \text{ A}$
Power supply voltage	220/380 V
Phase resistance	$R_s = 6.2 \text{ Ohm}$
Direct inductance	$L_d = 0.34 \text{ H}$
Quadrature inductance	$L_q = 0.105 \text{ H}$
Rated speed	1500 r.p.m
Maximum velocity	1800 r.p.m
Torque at rated velocity	7 Nm
Torque at maximum velocity	5.8 N m
Machine inertia	$J = 0.005 \text{ kg} \cdot \text{m}^2$
Viscous friction coefficient	$f = 0.01 \text{ Nm/s}$

References

1. Ashok, B.; Chidambaram, K.; Muhammad Usman, K.; Rajasekar, V.; Deepak, C.; Ramesh, R.; Narendhra, T.; Chellappan, K. Transition to Electric Mobility in India: Barriers Exploration and Pathways to Powertrain Shift through MCDM Approach. *J. Inst. Eng. (India) Ser.* **2022**, *103*, 1251–1277. [\[CrossRef\]](#)
2. Upadhyay, A.; Dalal, M.; Sanghvi, N.; Nair, S.; Scurtu, I.C.; Dragan, C. Electric Vehicles over Contemporary Combustion Engines. *Iop Conf. Ser. Earth Environ. Sci.* **2021**, *635*, 012004. [\[CrossRef\]](#)
3. El Hadraoui, H.; Zegrari, M.; Chebak, A.; Laayati, O.; Guennouni, N. A Multi-Criteria Analysis and Trends of Electric Motors for Electric Vehicles. *World Electr. Veh. J.* **2022**, *13*, 65. [\[CrossRef\]](#)
4. Rodríguez, E.; Rivera, N.; Fernández-González, A.; Pérez, T.; González, R.; Battez, A.H. Electrical compatibility of transmission fluids in electric vehicles. *Tribol. Int.* **2022**, *171*, 107544. [\[CrossRef\]](#)
5. Mohammad, K.S.; Jaber, A.S. Comparison of electric motors used in electric vehicle propulsion system. *Indones. J. Electr. Eng. Comput. Sci.* **2022**, *27*, 11–19. [\[CrossRef\]](#)
6. Gielen, D.; Lyons, M. *Critical Materials for the Energy Transition: Rare Earth Elements*; International Renewable Energy Agency: Abu Dhabi, United Arab Emirates, 2022; Volume 48.
7. Luo, X.; Qiu, Q.; Jing, L.; Zhang, D.; Huang, P.; Jia, S. Heavy Rare Earth Doped Nd-Fe-B Permanent Magnetic Material Performance Enhancement Methods and Their Motor Application Research. In Proceedings of the 2022 IEEE 5th International Electrical and Energy Conference (CIEEC), Nanjing, China, 27–29 May 2022; IEEE: New York, NY, USA, 2022; pp. 3121–3126.
8. Alves Dias, P.; Bobba, S.; Carrara, S.; Plazzotta, B. *The Role of Rare Earth Elements in Wind Energy and Electric Mobility*; European Commission: Luxembourg, 2020.
9. Singh, B.; Chowdhury, A.; Dixit, A.K.; Mishra, V.; Jain, A.; Kumar, N. Investigation on electric vehicle motor challenges, solutions and control strategies. *J. Inf. Optim. Sci.* **2022**, *43*, 185–191. [\[CrossRef\]](#)
10. Maciejewska, M.; Fuć, P.; Kardach, M. Analysis of electric motor vehicles market. *Combust. Engines* **2019**, *58*, 169–175. [\[CrossRef\]](#)
11. Heidari, H.; Rassölkin, A.; Kallaste, A.; Vaimann, T.; Andriushchenko, E.; Belahcen, A.; Lukichev, D.V. A review of synchronous reluctance motor-drive advancements. *Sustainability* **2021**, *13*, 729. [\[CrossRef\]](#)
12. Mohanarajah, T.; Rizk, J.; Hellany, A.; Nagrial, M.; Klyavlin, A. Torque Ripple Improvement in Synchronous Reluctance Machines. In Proceedings of the 2018 2nd International Conference On Electrical Engineering (EECon), Colombo, Sri Lanka, 28 September 2018; pp. 44–50. [\[CrossRef\]](#)
13. Muteba, M.; Twala, B.; Nicolae, D.V. Torque ripple minimization in synchronous reluctance motor using a sinusoidal rotor lamination shape. In Proceedings of the 2016 XXII International Conference on Electrical Machines (ICEM), Lausanne, Switzerland, 1–4 September 2016; pp. 606–611. [\[CrossRef\]](#)
14. Liang, J.; Dong, Y.; Sun, H.; Liu, R.; Zhu, G. Flux-Barrier Design and Torque Performance Analysis of Synchronous Reluctance Motor with Low Torque Ripple. *Appl. Sci.* **2022**, *12*, 3958. [\[CrossRef\]](#)
15. Li, X.; Wang, Y.; Qu, R. Design of synchronous reluctance motors with asymmetrical flux barriers for torque ripple reduction. In Proceedings of the 2021 IEEE 4th Student Conference on Electric Machines and Systems (SCEMS), Virtually, 2–3 December 2021; IEEE: New York, NY, USA, 2021; pp. 1–6.
16. Wu, H.; Depernet, D.; Lanfranchi, V.; Benkara, K.E.K.; Rasid, M.A.H. A novel and simple torque ripple minimization method of synchronous reluctance machine based on torque function method. *IEEE Trans. Ind. Electron.* **2020**, *68*, 92–102. [\[CrossRef\]](#)
17. Singh, A.K.; Raja, R.; Sebastian, T.; Rajashekara, K. Torque ripple minimization control strategy in synchronous reluctance machines. In Proceedings of the IECON 2021–47th Annual Conference of the IEEE Industrial Electronics Society, Toronto, ON, Canada, 13–16 October 2021; pp. 1–6.
18. Abou-ElSoud, A.M.; Nada, A.S.A.; Aziz, A.A.M.A.; Sabry, W. Synchronous Reluctance Motors Torque Ripples Reduction using Feedback Cascaded PII Controller. In Proceedings of the 2022 23rd International Middle East Power Systems Conference (MEPCON), Cairo, Egypt, 13 December 2022; IEEE: New York, NY, USA, 2022; pp. 1–5.
19. Moghaddam, H.A.; Vahedi, A.; Ebrahimi, S.H. Design Optimization of Transversely Laminated Synchronous Reluctance Machine for Flywheel Energy Storage System Using Response Surface Methodology. *IEEE Trans. Ind. Electron.* **2017**, *64*, 9748–9757. [\[CrossRef\]](#)
20. Yan, D.; Xia, C.; Guo, L.; Wang, H.; Shi, T. Design and Analysis for Torque Ripple Reduction in Synchronous Reluctance Machine. *IEEE Trans. Magn.* **2018**, *54*, 1–5. [\[CrossRef\]](#)
21. Gallicchio, G.; Palmieri, M.; Cupertino, F.; Di Nardo, M.; Degano, M.; Gerada, C. Design Methodologies of High Speed Synchronous Reluctance Machines. In Proceedings of the 2022 International Conference on Electrical Machines (ICEM), Valencia, Spain, 5–8 September 2022; pp. 448–454. [\[CrossRef\]](#)
22. Donaghy-Spargo, C.M. Electromagnetic–Mechanical Design of Synchronous Reluctance Rotors With Fine Features. *IEEE Trans. Magn.* **2017**, *53*, 1–8. [\[CrossRef\]](#)
23. Bianchi, N.; Degano, M.; Fornasiero, E. Sensitivity Analysis of Torque Ripple Reduction of Synchronous Reluctance and Interior PM Motors. *IEEE Trans. Ind. Appl.* **2015**, *51*, 187–195. [\[CrossRef\]](#)
24. Bonthu, S.S.R.; Tarek, M.T.B.; Choi, S. Optimal Torque Ripple Reduction Technique for Outer Rotor Permanent Magnet Synchronous Reluctance Motors. *IEEE Trans. Energy Convers.* **2018**, *33*, 1184–1192. [\[CrossRef\]](#)
25. Liu, H.C.; Kim, I.G.; Oh, Y.J.; Lee, J.; Go, S.C. Design of Permanent Magnet-Assisted Synchronous Reluctance Motor for Maximized Back-EMF and Torque Ripple Reduction. *IEEE Trans. Magn.* **2017**, *53*, 1–4. [\[CrossRef\]](#)

26. Huynh, T.A.; Hsieh, M.F.; Shih, K.J.; Kuo, H.F. An Investigation Into the Effect of PM Arrangements on PMA-SynRM Performance. *IEEE Trans. Ind. Appl.* **2018**, *54*, 5856–5868. [\[CrossRef\]](#)
27. Zhang, X.; Foo, G.H.B.; Vilathgamuwa, D.M.; Maskell, D.L. An Improved Robust Field-Weakening Algorithm for Direct-Torque-Controlled Synchronous-Reluctance-Motor Drives. *IEEE Trans. Ind. Electron.* **2015**, *62*, 3255–3264. [\[CrossRef\]](#)
28. Zhang, Z.; Liu, X. A Duty Ratio Control Strategy to Reduce Both Torque and Flux Ripples of DTC for Permanent Magnet Synchronous Machines. *IEEE Access* **2019**, *7*, 11820–11828. [\[CrossRef\]](#)
29. Mohan, D.; Zhang, X.; Beng Foo, G.H. Generalized DTC Strategy for Multilevel Inverter Fed IPMSMs with Constant Inverter Switching Frequency and Reduced Torque Ripples. *IEEE Trans. Energy Convers.* **2017**, *32*, 1031–1041. [\[CrossRef\]](#)
30. Li, C.; Wang, G.; Zhang, G.; Xu, D.; Xiao, D. Saliency-Based Sensorless Control for SynRM Drives with Suppression of Position Estimation Error. *IEEE Trans. Ind. Electron.* **2019**, *66*, 5839–5849. [\[CrossRef\]](#)
31. Ortombina, L.; Tinazzi, F.; Zigliotto, M. Adaptive Maximum Torque per Ampere Control of Synchronous Reluctance Motors by Radial Basis Function Networks. *IEEE J. Emerg. Sel. Top. Power Electron.* **2019**, *7*, 2531–2539. [\[CrossRef\]](#)
32. Truong, P.H.; Flieller, D.; Nguyen, N.K.; Merklé, J.; Sturtzer, G. Torque ripple minimization in non-sinusoidal synchronous reluctance motors based on artificial neural networks. *Electr. Power Syst. Res.* **2016**, *140*, 37–45. [\[CrossRef\]](#)
33. Singh, A.K.; Raja, R.; Sebastian, T.; Rajashekara, K. Torque Ripple Minimization Control Strategy in Synchronous Reluctance Machines. *IEEE Open J. Ind. Appl.* **2022**, *3*, 141–151. [\[CrossRef\]](#)
34. Moghaddam, R.R.; Magnussen, F.; Sadarangani, C. A FEM1 investigation on the Synchronous Reluctance Machine rotor geometry with just one flux barrier as a guide toward the optimal barrier's shape. In *IEEE Eurocon 2009*; IEEE: New York, NY, USA, 2009; pp. 663–670.
35. Agrebi, Y.; Triki, M.; Koubaa, Y.; Boussak, M. Rotor speed estimation for indirect stator flux oriented induction motor drive based on MRAS scheme JES. 2007. Available online: https://www.researchgate.net/profile/Youssef-Agrebi/publication/274892152_Rotor_resistance_estimation_for_indirect_stator_oriented_induction_motor_drive_based_on_MRAS_scheme/links/5a82c7860f7e9bda869fb0ce/Rotor-resistance-estimation-for-indirect-stator-oriented-induction-motor-drive-based-on-MRAS-scheme.pdf (accessed on 9 February 2023).
36. Xi, T.; Kehne, S.; Fey, M.; Brecher, C. Application of Optimal Control for Synchronous Reluctance Machines in Feed Drives of Machine Tools. In Proceedings of the 2022 International Conference on Electrical, Computer and Energy Technologies (ICECET), Prague, Czech Republic, 20–22 July 2022; pp. 1–6. [\[CrossRef\]](#)
37. Lubin, T. Modélisation et Commande de la Machine Synchrone à Réductance Variable: Prise en Compte de la Saturation Magnétique. Ph.D. Thesis, Université Henri Poincaré, Nancy, France, 2003.
38. Im, J.B.; Kim, W.; Kim, K.; Jin, C.S.; Choi, J.H.; Lee, J. Inductance Calculation Method of Synchronous Reluctance Motor Including Iron Loss and Cross Magnetic Saturation. *IEEE Trans. Magn.* **2009**, *45*, 2803–2806. [\[CrossRef\]](#)
39. Dilys, J.; Baskys, A. Self-identification of permanent magnet synchronous motor inductance for efficient sensorless control. In Proceedings of the 2017 Open Conference of Electrical, Electronic and Information Sciences (eStream), Vilnius, Lithuania, 27 April 2017; pp. 1–4. [\[CrossRef\]](#)
40. Dursun, D.C.; Yildiz, A.; Polat, M. Modeling of Synchronous Reluctance Motor and Open and Closed Loop Speed Control. In Proceedings of the 2022 21st International Symposium INFOTEH-JAHORINA (INFOTEH), East Sarajevo, Bosnia and Herzegovina, 16–18 March 2022; pp. 1–6. [\[CrossRef\]](#)
41. Bao, C.; Chen, H.; Yang, C.; Zhong, J.; Gao, H.; Song, S. Synchronous reluctance motor flux linkage saturation modeling based on stationary identification and neural networks. In Proceedings of the IECON 2022—48th Annual Conference of the IEEE Industrial Electronics Society, Brussels, Belgium, 17–20 October 2022; pp. 1–6. [\[CrossRef\]](#)
42. Santos, J.; Andrade, D.; Viajante, G.; Freitas, M.; Bernadeli, V. Analysis and Mathematical Modeling Of The Synchronous Reluctance Motor. *IEEE Lat. Am. Trans.* **2015**, *13*, 3820–3825. [\[CrossRef\]](#)
43. Hassan, M.R.M.; Mossa, M.A.; Dousoky, G.M. Evaluation of Electric Dynamic Performance of an Electric Vehicle System Using Different Control Techniques. *Electronics* **2021**, *10*, 2586. [\[CrossRef\]](#)
44. Deuskiewicz, P.; Radkowski, S. On-line condition monitoring of a power transmission unit of a rail vehicle. *Mech. Syst. Signal Process.* **2003**, *17*, 1321–1334. [\[CrossRef\]](#)
45. Minakawa, M.; Nakahara, J.; Ninomiya, J.; Orimoto, Y. Method for measuring force transmitted from road surface to tires and its applications. *Jsa Rev.* **1999**, *20*, 479–485. [\[CrossRef\]](#)
46. Liang, H.; To Chong, K.; Soo No, T.; Yi, S.Y. Vehicle longitudinal brake control using variable parameter sliding control. *Control. Eng. Pract.* **2003**, *11*, 403–411. [\[CrossRef\]](#)
47. Saadi, Y.; Sehab, R.; Chaibet, A.; Boukhni, M.; Diallo, D. Performance Comparison between Conventional and Robust Control for the Powertrain of an Electric Vehicle Propelled by a Switched Reluctance Machine. In Proceedings of the 2017 IEEE Vehicle Power and Propulsion Conference (VPPC), Belfort, France, 14–17 December 2017; pp. 1–6. [\[CrossRef\]](#)
48. Adhavan, B.; Kuppuswamy, A.; Jayabaskaran, G.; Jagannathan, V. Field oriented control of Permanent Magnet Synchronous Motor (PMSM) using fuzzy logic controller. In Proceedings of the 2011 IEEE Recent Advances in Intelligent Computational Systems, Trivandrum, India, 22–24 September 2011; IEEE: New York, NY, USA, 2011; pp. 587–592.
49. Diao, K.; Sun, X.; Bramerdorfer, G.; Cai, Y.; Lei, G.; Chen, L. Design optimization of switched reluctance machines for performance and reliability enhancements: A review. *Renew. Sustain. Energy Rev.* **2022**, *168*, 112785. [\[CrossRef\]](#)

50. Truong, P.H.; Flieller, D.; Nguyen, N.K.; Mercklé, J.; Sturtzer, G. An investigation of Adaline for torque ripple minimization in Non-Sinusoidal Synchronous Reluctance Motors. In Proceedings of the IECON 2013—39th Annual Conference of the IEEE Industrial Electronics Society, Vienna, Austria, 10–13 November 2013; IEEE: New York, NY, USA, 2013; pp. 2602–2607.
51. Truong, P.H.; Flieller, D.; Nguyen, N.K.; Mercklé, J.; Dat, M.T. Optimal efficiency control of synchronous reluctance motors-based ANN considering cross magnetic saturation and iron losses. In Proceedings of the IECON 2015—41st Annual Conference of the IEEE Industrial Electronics Society, Yokohama, Japan, 9–12 November 2015; IEEE: New York, NY, USA, 2015; pp. 004690–004695.
52. Utkin, V.; Lee, H. Chattering problem in sliding mode control systems. In Proceedings of the International Workshop on Variable Structure Systems, VSS'06, Alghero, Italy, 5–7 June 2006; IEEE: New York, NY, USA, 2006; pp. 346–350.
53. Dong, L.; Nguang, S.K. Chapter 5—Sliding mode control for multiagent systems with continuously switching topologies based on polytopic model. In *Consensus Tracking of Multi-Agent Systems with Switching Topologies*; Dong, L., Nguang, S.K., Eds.; Emerging Methodologies and Applications in Modelling; Academic Press: Cambridge, MA, USA, 2020; pp. 87–105. [\[CrossRef\]](#)
54. Shao, K.; Zheng, J.; Wang, H.; Wang, X.; Lu, R.; Man, Z. Tracking Control of a Linear Motor Positioner Based on Barrier Function Adaptive Sliding Mode. *IEEE Trans. Ind. Inform.* **2021**, *17*, 7479–7488. [\[CrossRef\]](#)
55. Edwards, C.; Colet, E.F.; Fridman, L.; Colet, E.F.; Fridman, L.M. In *Advances in Variable Structure and Sliding Mode Control*; Springer: Berlin/Heidelberg, Germany, 2006; Volume 334.
56. Bandyopadhyay, B.; Deepak, F.; Kim, K.S. *Sliding Mode Control Using Novel Sliding Surfaces*; Springer: Berlin/Heidelberg, Germany, 2009; Volume 392.
57. Saadi, Y.; Sehab, R.; Chaibet, A.; Boukhni, M.; Diallo, D. Sensorless control of switched reluctance motor for EV application using a sliding mode observer with unknown inputs. In Proceedings of the 2018 IEEE International Conference on Industrial Technology (ICIT), Lyon, France, 19–22 February 2018; pp. 516–521. [\[CrossRef\]](#)
58. Koshkouei, A.J.; Burnham, K.J.; Zinober, A.S. Dynamic sliding mode control design. *IEE-Proc.-Control. Theory Appl.* **2005**, *152*, 392–396. [\[CrossRef\]](#)
59. Lee, H.; Utkin, V.I. Chattering suppression methods in sliding mode control systems. *Annu. Rev. Control.* **2007**, *31*, 179–188. [\[CrossRef\]](#)
60. Dorel, L.; Levant, A. On chattering-free sliding-mode control. In Proceedings of the 2008 47th IEEE Conference on Decision and Control, Cancun, Mexico, 9–11 December 2008; IEEE: New York, NY, USA, 2008; pp. 2196–2201.
61. Levant, A. Sliding order and sliding accuracy in sliding mode control. *Int. J. Control.* **1993**, *58*, 1247–1263. [\[CrossRef\]](#)
62. Barth, A.; Reichhartinger, M.; Reger, J.; Horn, M.; Wulff, K. Lyapunov-design for a super-twisting sliding-mode controller using the certainty-equivalence principle. *IFAC-PapersOnLine* **2015**, *48*, 860–865. [\[CrossRef\]](#)
63. Utkin, V.; Guldner, J.; Shi, J. *Sliding Mode Control in Electro-Mechanical Systems*; CRC Press: Boca Raton, FL, USA, 2017.

Disclaimer/Publisher's Note: The statements, opinions and data contained in all publications are solely those of the individual author(s) and contributor(s) and not of MDPI and/or the editor(s). MDPI and/or the editor(s) disclaim responsibility for any injury to people or property resulting from any ideas, methods, instructions or products referred to in the content.